

7 March 2011

Kent H. Hughes
Satellite Oceanography and Climatology Division
Center for Satellite Applications and Research
NOAA/NESDIS
World Weather Building, Room 601
5200 Auth Road
Camp Springs, MD 20746

Menghua Wang
Marine Ecosystems Branch
Satellite Oceanography and Climatology Division
Center for Satellite Applications and Research
NOAA/NESDIS
World Weather Building, Room 601
5200 Auth Road
Camp Springs, MD 20746

Dear Mr. Hughes and Dr. Wang:

In accordance with the provisions of the Memorandum of Understanding (MOU) “Calibration Services for Marine Optical Buoy (MOBY) Operations” (MOU 18334), I am submitting the following annual report for the Optical Technology Division effort for the interval 01 October 2009 through 30 September 2010 and activity on the relevant amendments to the original MOU.

The document is organized according to specifics of the MOUs, including amendments. In addition, I mention some activities by NIST that are related to the MOBY Project but not specifically part of the MOUs. They are mentioned here for completeness.

Sincerely,

Carol Johnson, Physicist
Physical Measurement Laboratory
Optical Technology Division
Optical Thermometry and Spectral Methods Group
cc: Dr. Eric Shirley, Group Leader, Optical Thermometry and Spectral Methods

Calibration Services for Marine Optical Buoy (MOBY) Operations
Memorandum of Understanding between NOAA/NESDIS and NIST
Annual Report, Fiscal Year 2010 (October 1, 2009 to September 30, 2010)
C. Johnson, NIST

SECTION 1

Please reference Items 1 to 6 in the original MOU (effective April 16, 2008).

1. If the standard irradiance lamp operating hours, since the last calibration, exceed 50 hr, recalibrate at NIST two standard irradiance lamps for spectral irradiance in the range of 250 nm to 1600 nm. The Facility for Automated Spectroradiometric Calibrations-II (FASCAL-II) will be used.

There were no FEL lamps calibrated at NIST during the reporting interval.

2. If the integrating sphere lamp operating hours since the last calibration exceed 50 hr, recalibrate at NIST two standards of spectral radiance in the range 300 nm to 1000 nm. The Facility for Automated Spectroradiometric Calibrations (FASCAL) will be used.

There were no integrating sphere sources calibrated at NIST during the reporting interval.

3. Radiometric recalibration at NIST of the two portable, dual-purpose radiometers that were designed and built by NIST for establishing traceability to the MOBY Project (the Standard Lamp Monitors, or SLMs). The radiance and irradiance responsivity will be determined using the Spectral Irradiance and Radiance Calibrations with Uniform Sources (SIRCUS) facility. The radiometers were subjected to rough handling (a hard fall) on August 4, 2004 and the next recalibration cycle must include thorough inspection and repair before any measurements are performed.

The SLMs were not calibrated at SIRCUS during the reporting interval.

4. The SIRCUS calibration of the SLMs will be validated by measurement of NIST standard radiance and irradiance sources, calibrated at NIST using FASCAL or FASCAL-II, in the Remote Sensing Laboratory at NIST.

In September, 2010, the SLMs in radiance mode measured the NIST Portable Radiance (NPR) source in the Remote Sensing Laboratory at NIST. This was prior to their scheduled deployment on the NIST SIRCUS facility. Also in September 2010, the SLMs in irradiance mode measured three NIST calibrated FEL standard irradiance lamps, F187, F431, and F432, also prior to their scheduled deployment for calibration on the NIST SIRCUS facility.

5. Participate in on-site calibration activities at Snug Harbor in Honolulu, Hawaii. The on-site calibration activity will involve two NIST scientists and will consist of verifying the radiance of the on-site standards. With the consent of the Earth Observing Satellite (EOS) calibration scientists, the Visible Transfer Radiometer (VXR) and the NIST

Portable Radiance (NPR) source would be used on-site to compare the standards used for MOBY. The VXR is used for similar validation measurements with other EOS sensors.

The VXR and the NPR were deployed to the MOBY Facility in Snug Harbor, Honolulu, Hawaii, from 13 to 16 December, 2009. Measurements were made using the VXR and the SLMs of the NPR and the MLML/MOBY calibration sources – the MML OL420 and MLML OL425.

6. Semi-Annual progress report describing tasks funded by this agreement. The first report is due 6 months after receipt of the funds.

SECTION 2

Please reference Amendment 3 to the original MOU, effective June 3, 2010 regarding the stray light characterizations done at NIST in 2008 for the Even (MOS204) and Odd (MOS205) buoys. This report was submitted to NOAA/NESDIS as a separate document in September 2010 but it is included here for completeness.

Stray Light Correction for the Marine Optical Buoy
MOBY Science, Updated September 2010
Carol Johnson, NIST

A known bias in the MOBY data is stray light. Under a NIST-led effort, laser characterization data were acquired at the Snug Harbor facility in the early 2000's and a stray light correction algorithm developed and implemented – the version release is January 2005. Starting in 2005, it became obvious the stray light performance of the sensors in MOBY was changing with time. We currently estimate the retrievals for Lu could be in error by as much as 5% at 412 nm. In 2008 the systems were characterized at the NIST SIRCUS facility (in June for the odd buoy and November for the even buoy). Hundreds of scans were obtained over about 25 days of laboratory measurements. There are four spectrographs (two each in the odd and even buoys), and eight input collectors, for a potential total of 32 independent stray light correction matrices. A detailed set of laser observations were acquired at about every 5 nm for LuTOP and LuMOS and for a subset of these wavelengths, observations were acquired about every 30 nm for LuMID, LuBOT, Es, and the three Ed channels. The work that must be done for this data set is: 1) the analysis of the full set of laser observations (data massaging, quality checking, development of the correction matrix) for LuTOP; 2a) implementation of item 1 for LuMOS and 2b) assessing the results for all the other channels to confirm that the LuTOP matrix can be used for all the fiber-coupled inputs; 3) validate matrix results (the code and the algorithm itself) by implementing alternate techniques; 4) test on 2008 *in situ* MOBY data (buoy 241 and 242) and compare to the existing SLC method; 5) validate the new method with CIE color coordinate analysis of buoy 241 and 242 Es results and the use of specialized validation sources at the MOBY site (filtered white light sources, polychromatic and monochromatic sources (LEDs, emission lamps, lasers); and 6) publish results. Without this effort, the reported MOBY results are compromised from 2005 and beyond and it is not possible to state that they are meeting the uncertainty requirements necessary for the end users. Completion of this effort is a requirement before an effort to evaluate and correct for stray light during the different instrument epochs of behavior can be approached. Note such implementation is outside the scope of work given the limited resources, but we have submitted a separate proposal to NASA to do this work

September 9, 2010

Progress Report

The Year 1 (FY2010) \$40k arrived at NIST July 1, 2010. First, we are determining how to generate a stray light matrix from the 2008 SIRCUS data sets that we trust. This involves data sets that have random and systematic noise, multiple, complicated features, and inconsistencies (e.g., dark scans greater than light scans). We have developed a novel cumulative integration, interpolation, and differentiation approach that has the potential to more fully automate the interpolation part of the procedure and more accurately treat the many small but broad and

significant features.

Item 1: All of the LuTOP data sets have been examined, and the analysis has been finalized for the Even Blue spectrograph LuTOP, with some work remaining for Even Red LuTOP. The odd buoy data are more problematic, with poor repeatability and darks greater than lights for some scans, thus requiring judgment and time consuming evaluation and considerations. The analysis of how to fix the problematic scans for the LuTOP blue spectrograph data is done. Once the fixes have been applied the matrix will be finished. We are still working on the red spectrograph matrix for the odd buoy.

Item 2a: The LuMOS channel, being non-fibered, has trapezoidal, not curved, shapes in the reflection peaks, so these data must be treated separately – these matrices are yet to be developed.

Item 2b: All of the other fibered channel data have been examined, and in some cases for the odd buoy, used to sort out the observed inconsistencies in the data.

Item 3: In collaboration with the NIST Statistical Engineering Division, we have investigated alternative stray light correction algorithms that are based on maximizing a likelihood function, and concluded that this method would be difficult to implement. We have also developed a new way to examine the intermediate results of the stray light correction algorithm in order to determine which features in the stray light matrix are the most significant.

Item 4: This study of 2008 MOBY data will begin once the stray light matrices are finalized.

Item 5: A remaining measurement is to acquire a high accuracy validation data set – by validation we mean MOBY LuTOP measures a second calibrated source, one that has comparable spectral distribution to the Lu spectra at the MOBY site; an outstanding need is to improve on the filtered OL420 integrating sphere measurements that have been done to date by use of alternative sources such as LEDs.

Item 6: We will publish this work, consisting of description of MOBY SIRCUS measurements, analysis of these data, description of validation data, estimation of the uncertainties, and impact on the MOBY deployments 241 and 242.

Summary, Year 1

The Year 1 Milestone:

Develop a new MOBY stray-light correction matrix based on 2008 SIRCUS characterizations. As described above, we have developed stray-light correction matrices with differing levels of maturity for complete systems. Before implementing these results into operational processing, additional effort is required, as described herein.

Year Two funding is requested at the level of \$50k to complete this work.

The work to be done is described above in items 1, 2, and 4 to 6. Item 3 is complete and Item 1 is well underway. The LuMOS data will be used to create stray light matrices, we will apply these matrices to buoys 241 and 242, acquire the validation data using the buoy in operation at the time of these measurements, assess the uncertainties in the stray light correction, and analyze the data and write the archival paper. The acquisition of the validation data will require a trip to Honolulu by NIST staff, and the preparation of an appropriate calibrated validation source to serve as the test standard. It should be noted this work is time critical as the Marine Optical Systems (MOSs) that contain the spectrographs will be serviced soon. Changes in the stray light performance for past deployments are associated with these servicing exercises, where the optics

are exposed to ambient conditions have high humidity. This will make it difficult to interpret 2010 validation data for a 2008 system as characterized at NIST on SIRCUS.

The Year 2 Milestone:

Validate the new MOBY stray-light correction matrix using colored sources and other methods, estimate and assign uncertainties in the stray-light correction for 2008 MOBY deployments, and publish these results.

SECTION 3

Please reference Amendment 2 to the original MOU, effective April 30, 2009 regarding the multi-input fiber-coupled spectrograph approach. This design has been recommended by NIST and MLML for replacing the optical system in the existing MOBY. NASA, through a ROSES 2006 proposal, funded the development of the hardware. The funding supplied by NOAA in Amendment 2 is for characterization and development of the instruments as field-deployable oceanographic instruments. A detailed final report was submitted to NASA at the end of the ROSES2006 effort and it is included here as Appendix 2.

The work at NIST began with testing of the blue Resonon in November 2009. We assessed the camera performance, including noise performance issues. In December 2009, the blue Resonon was put on SIRCUS for stray light characterization. This showed the instrument design is superb for ocean color research. An artifact caused by a ghost reflection in the grating was identified, but this can be eliminated in future implementations. NIST presented the results at the January 2010 MODIS/VIIRS Ocean Color Science Team Meeting in Washington, DC.

Moss Landing Marine Laboratories, Mark Yarbrough, PI collaborated on the project via a grant from NIST, are responsible for the integration of the blue and red spectrograph units as field oceanographic radiometers. The two institutions work closely together, with NIST participating in some testing of the red Resonon during the December 2009 VXR/NPR deployment. NIST also provided some optical design support for the shutter block assembly. The MLML activities are described in detail in Appendix 1.

SECTION 4

NIST participated in other activities not outlined in the MOU that were relevant to the MOBY Project. The support provided helped ensure the necessity of the MOBY facility for VIIRS. A key meeting was the attendance and presentation at the NRC Ocean Color Studies Board, in Irvine, California (June 2010). NIST, with Carol Johnson as PI, submitted a proposal to NASA's ROSES 2010 NRA (April 2010).

APPENDIX 1
Fiber Optic Ocean Color Sensor Development
Mark Yarbrough, MLML, PI

In accordance with the provisions of my NIST Grant (Foundation Account Number 21-1509-4207, NIST# 70NANB8H8113), I am submitting the following Annual Report. This Report covers the Moss Landing Marine Laboratories portion of this grant completed through 14 August 2010. The primary objective of this year's effort involved fabrication and assembly of the underwater housing, optics and support electronics for the MIFS spectroradiometer system. MLML personnel continue to work with NIST on optical characterizations of the Blue and Red spectrograph systems. We also continue to support work on stray light correction methods as they apply to these new systems.

23 October 2010

Moss Landing Marine Laboratories (MLML) activities for our "*Fiber Optic Ocean Color Sensor Development*" grant. Covering the MLML team activity through 14 August 2010.

During the past year of this Grant we have worked closely with NIST personnel in developing a high performance, fiber optic coupled spectroradiometer system. This work is part of an ongoing effort to improve the state of the art in Ocean Color Science as applied to in-water radiometry and the determination of water leaving radiance for use in Ocean Color Satellite Vicarious Calibrations (ViCal). The primary task of the current grant is delivery of an underwater housing and support electronics for the MIFS radiometer system. Our efforts this year can be broken down into three areas: 1) Spectrograph under water housing, 2) Measurement science, 3) Collection optics.

Underwater housing

The housing design is complete and most parts have been delivered. The full assemble is shown in Appendix 1. The pictures show only the housing elements as both spectrograph systems are currently at NIST for optical work (Appendix 2). The exterior heat sink elements are not pictured since we are awaiting delivery on these items.

Measurement Science

Stephanie Flora and Mike Feinholz continued their work with Carol Johnson, Steve Brown and others at NIST to characterize the optical performance of the new in-line VPH spectrographs systems. Much of this work entails low lever characterization of the CCD performance and initial stray light analysis using data provide by SIRCUS measurements at NIST. Stephanie is developing MatLab data analysis tools to support our optical characterization work and to apply the results in correcting the spectrograph output. Results from the optical work are too voluminous to include in this report. The full findings are archived at http://data.moby.mlml.calstate.edu/moby2_testing/sudirlsit.html

Collection Optics

We are currently investigating the characteristics and performance of bare fiber optic collection

optics. We have also designed a collimated optical collector as for radiance measurement. Work is continuing on the design of a small in-water irradiance collector, which will be a scaled down version of the existing MOBY collector.

Remaining work

Shutter controller

The shutter control electronics are designed and we are waiting delivery of circuit boards to finish assembly of this item.

MIFS-R optical characterization

This unit is now at NIST for this work.

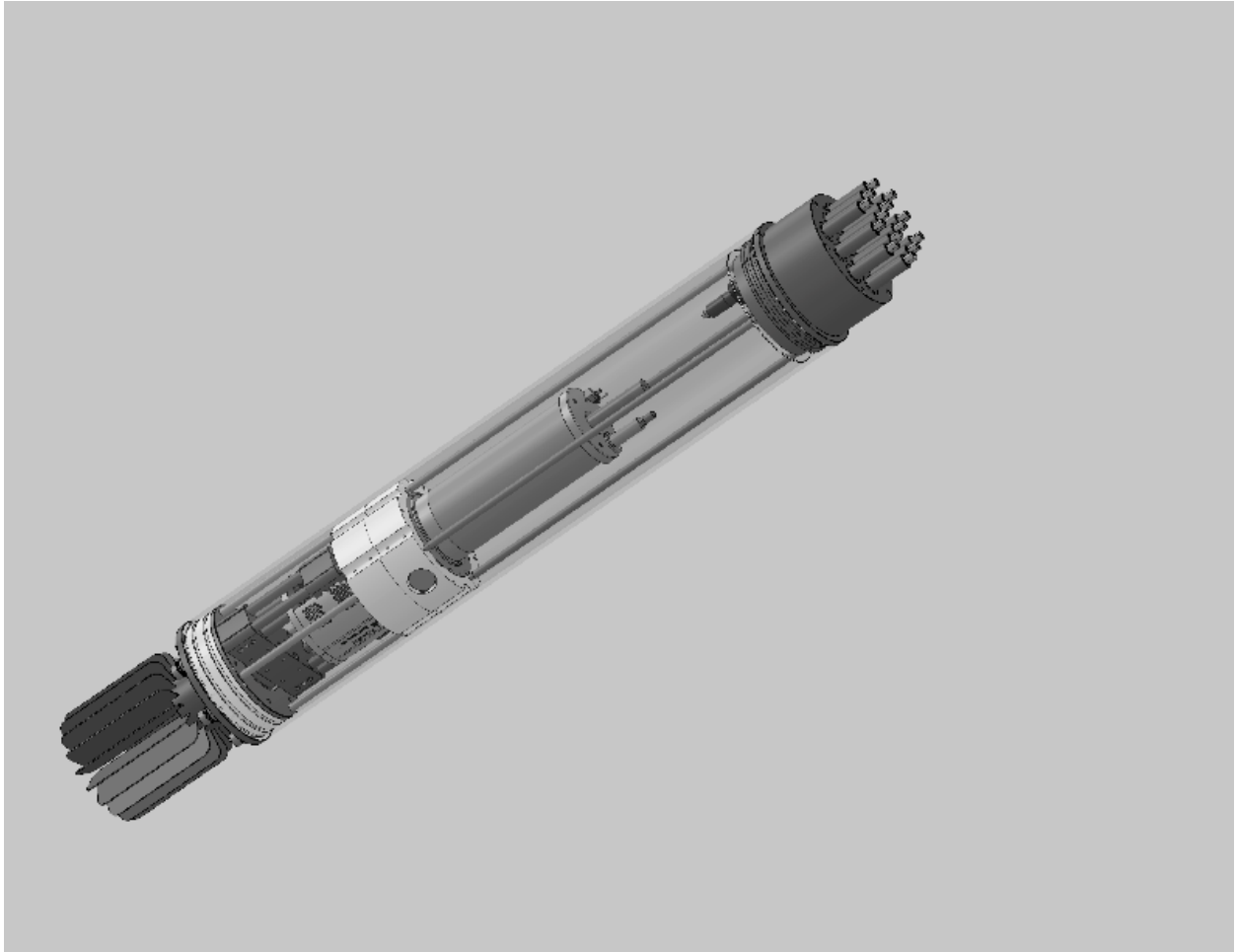
MIFS-B PGP replacement

The PGP has been redesigned to eliminate a ~400 nm reflection peak caused by a refractive index mismatch in the PGP element optical adhesive. The new part is being ordered by NIST and will be installed by Resonon. The SIRCUS characterizations will be repeated upon delivery of the repaired system.

No-cost extension

I have requested a no-cost extension for the period of one year. During this time we will complete the underwater housing assembly and complete the optical characterization work at NIST. I am requesting that this remaining work be covered under a no-cost extension to allow the MLML personnel to remain under contract, allowing us to utilize the remaining travel and salary funds during the next year for this work.

Appendix 1: Underwater spectroradiometer system.



Rendering of MIFS radiometer system in the underwater housing.



Internal housing frame (outer tube removed, MIFS radiometer not installed)



Housing exterior with outer tube installed



Fiber optic input connector block



Collimators, Shutter block, Widow end cap and Sealed F.O. connectors, 14 input fiber optics



Spectrograph side, 14 collimators with iris



Sealed fiber optic connector with fiber collector and cable jacket seal



Housing connector end cap and CCD heatsink (external radiator fins not installed)

APPENDIX 2
Final Report on ROSES 2006 Award
To: Dr. Paula Bontempi, NASA HQ, Washington, DC

New Sensor Technology for Ocean Color Vicarious Calibration
February 21, 2008 to February 21, 2010

Interagency Agreement to NIST #NNH08AH65I
“Advanced Hyperspectral Autonomous Buoy for Accurate Vicarious Calibration of Ocean Color
Sensors: A Necessity for Climate Data Records of Water-Leaving Spectral Radiance,”
NRA NNH06ZDA001N, Proposal Number 06-EOS/06-114

Carol Johnson, PI, NIST

Introduction and Background

The Marine Optical Buoy (MOBY), developed by Dennis Clark, has served the space based remote sensing community for a number of years, with support initiated by NASA and augmented by NOAA, see Clark *et al.* 2003 for more information on the instrument and facility. MOBY supplies values of the water-leaving radiance for use by satellite sensors to vicariously calibrate ocean color sensors, see Franz *et al.* 2007 for a description of this process. It is recognized by the ocean color community that MOBY serves an essential function and that the instrument is approaching its practical lifetime. Our 2006 proposal to the ROSES 2006 “Earth System Science Research Using Data and Products from the Terra, Aqua, and ACRIMSAT Satellites” requested \$5.5M over three years to develop a completely new facility and optical system. Included in this budget was a projected shortfall to cover NOAA’s maintenance and operation of the original system over this time interval. NASA decided to provide support, but at a greatly reduced amount (\$200k) and for one year only. A revised statement of work was submitted in December 2007 that focused solely on research, development, and evaluation of an optical sensor design that was deemed suitable as the replacement operational sensor for the next generation MOBY or for any other vicarious calibration site or facility. A single instrument was proposed, with spectral coverage in the red (550 nm to 950 nm). The reduced scope of activities compared to the original proposal still required partnership with Clark and the Moss Landing Marine Laboratories (MLML) but eliminated the roles of Co-Is Kenneth Voss (U. Miami) and Menghua Wang (NOAA). NOAA has been successful in maintaining MOBY operations since 2007, but secure funding to replace the aging system is not yet identified. However, in FY09 \$200k was allocated to NIST by NOAA to further the development of the new sensor; the status of this work is mentioned briefly in our concluding remarks. Our efforts as outlined in the ROSES 2006 revised statement of work have been successful and here we report the results. The opportunity exists to utilize this design in an updated version of the MOBY facility that would take advantages of the new sensor technologies to improve the MOBY-supplied data.

The MOBY facility uses a separate spectrograph for the blue and red spectral regions. They are integrated into a single unit, with a dichroic beamsplitter directing flux from the sources into both systems simultaneously. The intermediate coupling from the different source input

channels that are required for the determination of water-leaving spectral radiance (e.g., different depths for up-welling radiance) is fiber coupled for all but one input, and a rotating mirror assembly sequentially aligns the input to the spectrographs to these channels (Clark *et al.* 2003). Thus the instrument loses efficiency by the necessity of only viewing a single channel at a time. The viewing conditions can change during the course of a sequence and this necessitates considerable data gathering chores to correct for background and incoming irradiance changes. An advantage of making simultaneous measurements is a reduction in the uncertainty because a prime source of noise is natural variability, affecting all channels at the same time. A second advantage is the number of samples (length of the acquisition time) can be optimized for reduction of random noise; this is not possible in the current MOBY approach because determination of the water-leaving radiance from the multiple inputs restricts the total time interval for a complete measurement set.

In 2005 funding became available at NOAA for “Research to Operations” and we applied this resource to study a multi-channel, simultaneous, hyperspectral sensor approach (Yarbrough *et al.* 2007). Two systems were tested – a breadboard system constructed using existing equipment, and a purchased commercial off-the-shelf (COTS) spectrograph that used a novel grating design. As a result, in our ROSES 2006 proposal, the team suggested a redesign of the MOBY sensor system for this type of buoy operation that would incorporate a hyperspectral imaging spectrograph with the simultaneous measurement of all the necessary sensor channels needed to determine the water-leaving spectral radiance. This report describes the design and initial characterization of two new instruments that could prove to be a significant improvement for the data gathering tasks involved.

Design and Instrument Specifications

The impetus for this project was to seek a new design for the spectrographs to be used in the building of an instrument to replace the spectrographs on the MOBY system. The present sequential operation measures the various MOBY radiance and irradiance sensors individually and as a consequence the results must be normalized to account for time varying factors such as incoming solar irradiance. The new instrument system would seek to take advantage of the rapid advances in hyperspectral imaging made possible by the ready availability of high quality CCD detectors and volume phase holographic transmissive gratings. The concept is to direct the flux from the various radiance and irradiance collectors simultaneously to the entrance slit of a spectrograph system by mounting the fiber optics directly to the entrance slit. The spectrograph would then image the spectra furnished by the fibers to displaced bands in the image plane of the spectrographs and hence the CCD array could simultaneously gather all the necessary spectra to furnish a MOBY data product for water leaving radiance.

A further design consideration was to pursue an optical design that would seek to minimize the stray light in the spectrographs and yet maintain a compact system for ease of field deployment. The breadboard system mentioned above was a Jobin Yvon (JY) CP140 spectrograph¹ coupled

¹ Certain commercial equipment, instruments, or materials are identified in this paper to foster understanding. Such identification does not imply recommendation or endorsement by the National Institute of Standards and Technology, nor does it imply that the material or equipment is necessarily the best available for the purpose.

to an Andor CCD detector, and the COTS system was a Kaiser Optical Systems, Inc. (KOSI) Holospec model spectrograph that used a flat volume phase holographic transmissive grating and an Apogee Alta CCD camera. With the experience gained (see Yarbrough *et al.* 2007), NIST solicited ideas and inputs from potential vendors to develop a multiple input spectrograph system. Key requirements in addition to the stray light and imaging performance were a compact, linear design for ease of implementation into autonomous field hardware, thermal and radiometric stability, and insensitivity to the harsh marine environment. Investigation led to the decision that the optimal design ideas were from Resonon, Inc., a manufacturer of custom optical instruments. Due to the performance of optical components, the team decided to design two separate spectrographs, one for the blue portion of the spectra (370 nm to 720 nm) and one for the red portion of the spectra (500 nm to 900 nm). This provides an ample wavelength overlap interval to compare the two instruments. The revised statement of work explained we would supply the red spectrograph and perform field testing similar to that executed with the CP140 and Holospec systems. However, Resonon preferred to supply both spectrographs in hardware as a single procurement, and we agreed this was the most economical approach. For this reason, the field testing, which involved small boat operations off the coast of O'ahu, was deferred for later.

When deployed as an ocean color vicarious calibration facility, we envision using two optical fibers for every single one used in the MOBY design. The dichroic beamsplitter that feeds the two MOBY spectrographs from a single fiber is replaced by separate optical fibers for each of the new spectrographs. This is not the only possible implementation, but would mean that the depths of the various channels could be optimized for each spectral region. This is an important consideration for marine optics, where the optical depths are strongly dependent on the spectral absorption and scattering properties of seawater and its constituents. The sensor described here is flexible and can be optimized for the specific measurement conditions, from the MOBY Case 1 waters (scattering dominated in the blue spectral region) to complex coastal waters (absorption often dominates scattering in the blue spectral region).

Resonon developed a new design for an instrument based on our specifications. It is hyperspectral and images 14 fiber optic input channels simultaneously (800 μm core fiber optic core diameter). The assembled spectrograph and CCD camera is less than 15.2 cm (6") in diameter and 43.2 cm (17") long. The optical design is based upon a double-prism single transmission grating concept with all the optical components being on a single optical axis. A cut away diagram is shown in Figure 1.

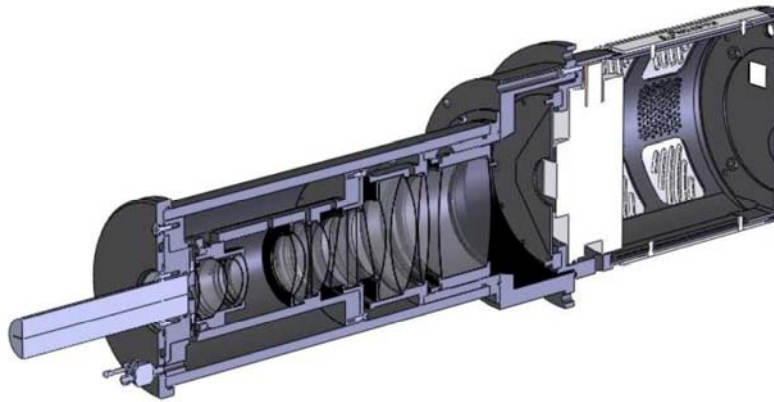


Figure 1. Cut away drawing of the Resonon spectrograph. The fiber optic bundle (on the left) is mated to the entrance slit. The light is directed to the prism-grating configuration and then the dispersed radiation is imaged on the CCD array camera (on the right).

Cut away drawings of the two optical systems are shown in Figs. 2 and 3. The first set of lenses collimates the light from the entrance slit which is then directed to the prism-grating-prism (PGP) sector. After dispersion the light is then focused on the CCD. The optical systems of both the blue and red spectrographs were designed so that common elements could be used in both as much as possible, see Appendix A. The antireflection coatings were designed to provide optimal throughput for the particular wavelength region.

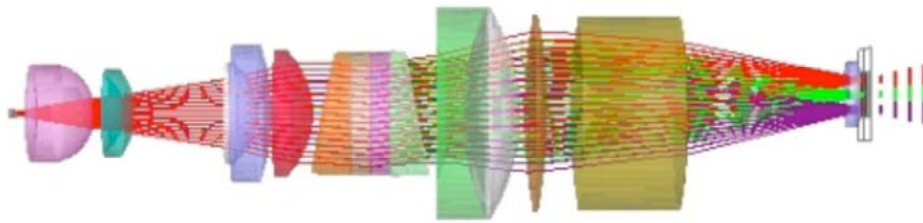


Figure 2. Cross section of the optical elements of the blue spectrograph. The entrance slit is on the left and the CCD array is on the right.

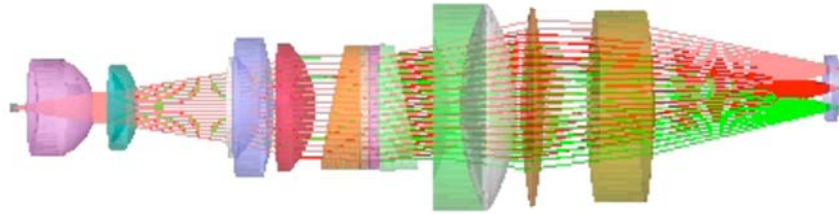


Figure 3. Cross section of the optical elements of the red spectrograph. The entrance slit is on the left and the CCD array is on the right.

A cursory inspection indicates the similarity of the optical design and layout and hence the expected similarity of performance and use. The final Resonon report to this project (Kehoe and Dodge 2009) was modified to remove competition-sensitive material and is attached to this report as Appendix A. The CCD cameras are commercial instruments manufactured by Princeton Instruments; model PIXIS 1024B for the blue spectrograph and model 1024BR for the red spectrograph. The physical dimension of these cameras supports the in-line design, the CCD hardware supports on-chip binning that results in improved signal-to-noise ratios over the full dynamic range, and the dual readout speeds and multiple gain settings are standard. The overall spectrograph parameters are given in Table 1 adapted from the Resonon report and reproduced here for convenience.

Table 1: Key Characteristics of Blue and Red Imaging Spectrographs		
Characteristic	Blue	Red
diameter	9.9 cm (spectrograph) 13.7 cm (mounting flange)	9.9 cm (spectrograph) 13.7 cm (mounting flange)
Length	41.7 cm (not including connectors or fiber bundle)	43.2 cm (not including connectors or fiber bundle)
wavelength range	370-720 nm (optimized from 390-720 nm)	500-900 nm
size of image	13mm x 13 mm	13 mm x 13 mm
silt dimensions	13 mm x 25 μ m	13 mm x 25 μ m
mechanical component material	6061 aluminum	6061 aluminum

The entrance slit to the spectrograph is a curved slit of 25 μ m width and is designed to minimize distortion of the optical system. The entrance slit is mated to a fiber optic assembly (Romack, Inc.) which has 14 individual fibers of 800 μ m core diameter. At the slit end, the individual fibers are secured in a linear configuration; they are separate at the other end so as to form

different input channels. Light from the fibers is dispersed and then imaged by the spectrograph system. The lens system collimates the light from the entrance slit onto the PGP element and upon dispersal focuses it on the CCD array in the image plane with near unity magnification. Due to off-axis aberrations in the optical system distortions will be greater for the fiber bundles imaged further from the central axes. These effects are mitigated to some extent by the curved slit mentioned earlier and will be dealt with in the calibration procedure.

An example of the simultaneous acquisition of spectra is shown in Fig. 4. This figure shows a test spectrum taken by illuminating all the fiber bundles with a white light source and is presented as an example of how the data are to be accumulated with this device. The horizontal axis is the pixel count number, which is in the dispersion direction, and the vertical axis is the pixel count number, which is in the slit height direction. It shows the 14 spatially displaced spectra separated by a gap that is dependent upon the fiber spacing on the entrance slit. These individual spectra on the CCD are referred to as “tracks” and are identified sequentially beginning with CCD row zero. The alignment is not ideal in the along slit direction, so Track 14 is partially off the CCD. Also, there is a decreased sensitivity for Track 12 that could be related to a damaged fiber in the input bundle. The challenge is to characterize the spectrograph system such that the intensities of the light in each of the tracks can be calibrated with a known standard and that the radiances and irradiances they represent on a system like MOBY can be used to generate the scientific product of water-leaving radiance.

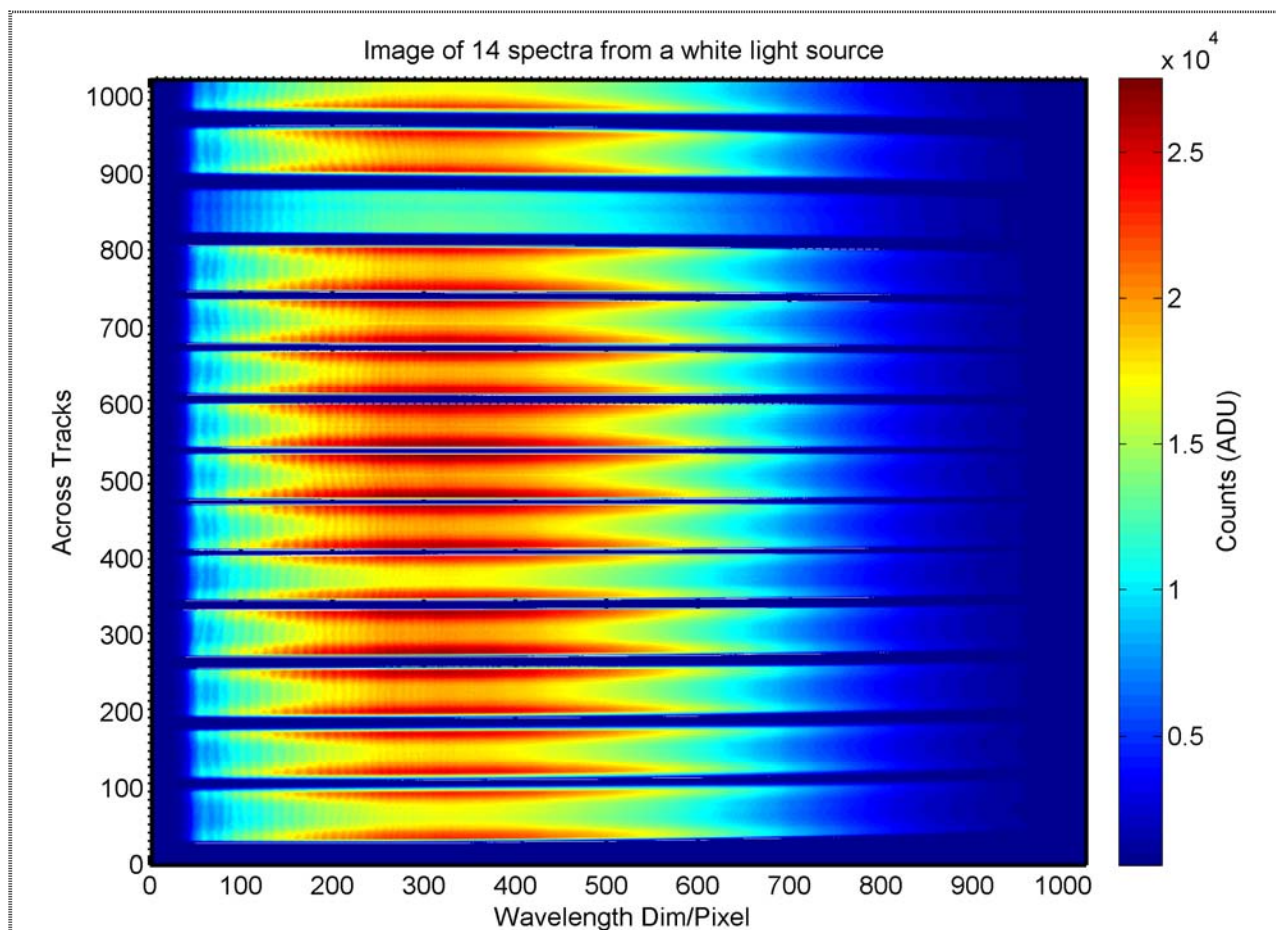


Figure 4. Sample image of the simultaneous acquisition of 14 spectra from a white light source that illuminated all fibers. The horizontal axis is in CCD columns (pixels) and is in proportion to wavelength; the vertical axis is CCD rows (pixels) and is in proportion to physical location along the long axis of the entrance slit. The individual fiber-illuminated sections are termed “tracks” and are numbered from 1 to 14 starting at the bottom of the image; spectra go from red to blue with increasing pixel values.

Characterization and Performance

The information on Fig. 4 indicates the general function of the Resonon instrument in that it simultaneously can accumulate all 14 tracks of data. The characterizations reported here have centered on understanding the imaging in the dispersion and slit dimensions, including stray light and cross track illumination. The stray light and cross track testing was performed at the NIST Spectral Irradiance and Radiance Calibration with Uniform Sources (SIRCUS) facility (Brown *et al.* 2000). A reflection artifact that needs attention was noted in the blue spectrograph and it is illustrated in Fig. 5. A key observation was that the position of the artifact in the dispersion direction was independent of the wavelength of the incident flux, indicating that the artifact involved zero-order dispersion in some fashion. In Fig. 5, Track 2 was illuminated and the artifact occurs primarily on Track 13. The problem appears in every track in a complementary way, Track 1 and Track 14, Track 3 and Track 12 and so on.

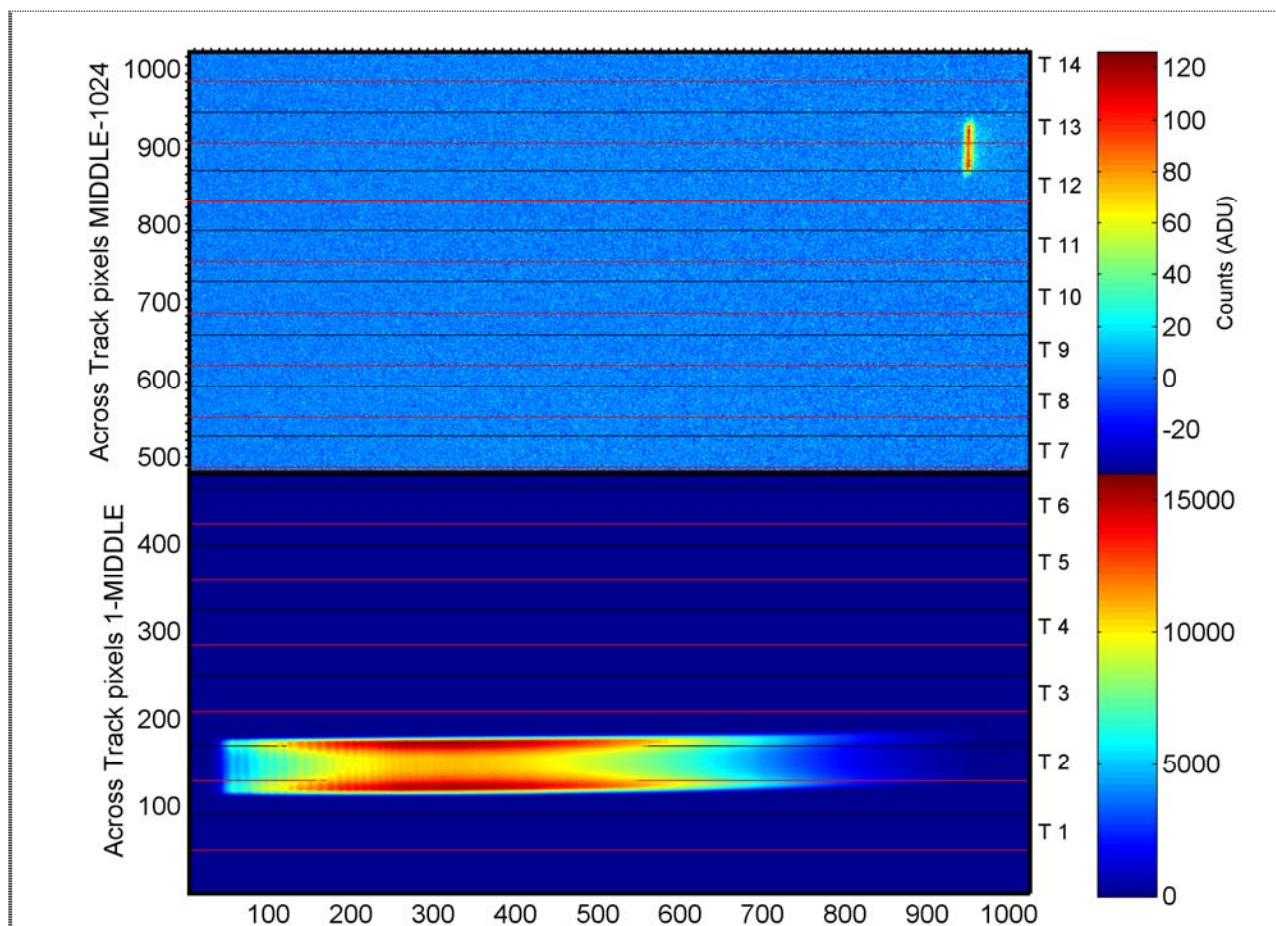


Figure 5. With one track illuminated (in this case Track 2), a spurious image appears on the track that is symmetric with the illuminated track about the center of the image plane (in this case Track 13). Note the change in scale for the lower and upper regions of the image. The solid horizontal lines correspond to the defined track boundaries, with black for the top of the track and red for the bottom of the track; the width of each track including the adjacent gap is about 70 pixels.

This artifact only occurs in the blue instrument and was not predicted in the original modeling by Resonon, which included studies of interreflections and the effects of stray light. Discussions of the test results and subsequent optical modeling by Resonon provided the explanation: the CCD array reflects a portion of the dispersed flux back to the PGP assembly, where it is recombined spectrally, reflected off a particular surface back through the PGP assembly, and then the zero-order component is focused onto the image plane. This mechanism correctly predicts the observed symmetries of the artifact as a function of which track is illuminated. The surface causing the back reflection is where an additional SiO₂ coating was applied during the production of the blue PGP component as a precaution to ensure its stability during the manufacturer and assembly process. This step is not necessary; the coating is not a required element of the optical design. The artifact overlaps with the 412 nm ocean color band and the zero-order nature of the effect enhances the impact because all flux in an observed broadband

source contributes to this undesired signal. Two solutions are possible – development of specific correction algorithms for this artifact that would operate in addition to the standard stray light correction algorithm (Zong *et al.* 2006) or replacement of the PGP assembly in the blue spectrograph with one that is manufactured without the SiO₂ coating.

The SIRCUS testing indicated that the stray light rejection on this instrument was very good in comparison to the Marine Optical System (MOS) that is used in MOBY, as well as the two other multi-channel instruments mentioned above – the Holospec and the CP140. Figure 6 shows the output of one of the channels (tracks) on the Resonon instrument compared to these three other imaging spectrograph systems. Inspection of Fig. 6 indicates that the out-of-band response to similar laser illumination is nearly an order magnitude less on the Resonon instrument compared to the other instruments. In the wings of the peak, the signal is down by 5 orders of magnitude for the Resonon spectrographs and hence the stray light correction will be significantly less for this instrument compared to the MOBY spectrographs and the other instruments compared in Fig. 6. Particularly for the MOS instrument the decrease in out-of-band or stray light is quite significant, about a factor of 20. Absent also from the Resonon instrument is the complexity of secondary peaks that are a cause of stray light removal difficulty with the MOBY instrument as can be seen on the MOS output in Fig. 6 or in the results presented in Feinholz *et al.* (2009).

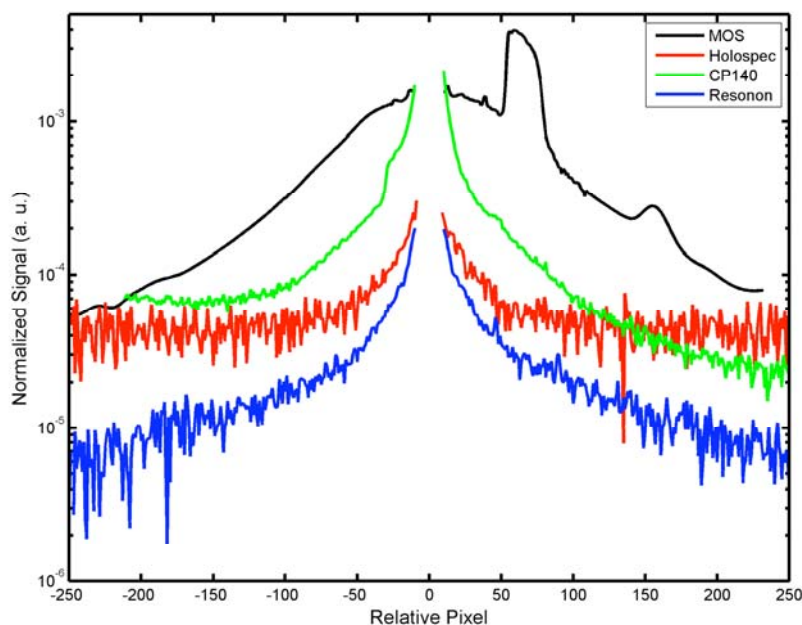


Figure 6. Comparison of the output of the blue Resonon instrument to a JY CP140, a KOSI Holospec, and a MOBY MOS spectrograph using monochromatic laser illumination. The signals have been normalized by the in-band area (delineated by the gap near relative pixel zero) and shifted in pixel (wavelength) coordinate in order to emphasize the differences in the wings; finite response away from the central peak with monochromatic illumination is termed “stray light” and causes spectral biases in the data.

This initial stray light characterization data with the SIRCUS facility was limited in scope. A coarse input laser wavelength grid of 40 nm was used for Tracks 6 and 8; 20 nm for Track 7; the remainder of the tracks were measured at a single wavelength of 550 nm. These initial data, see Fig. 7, are adequate to evaluate the overall optical performance. A concern with the inline design was ghosting and ubiquitous reflections – the Resonon modeling indicated there should not be any problems and the data support this.

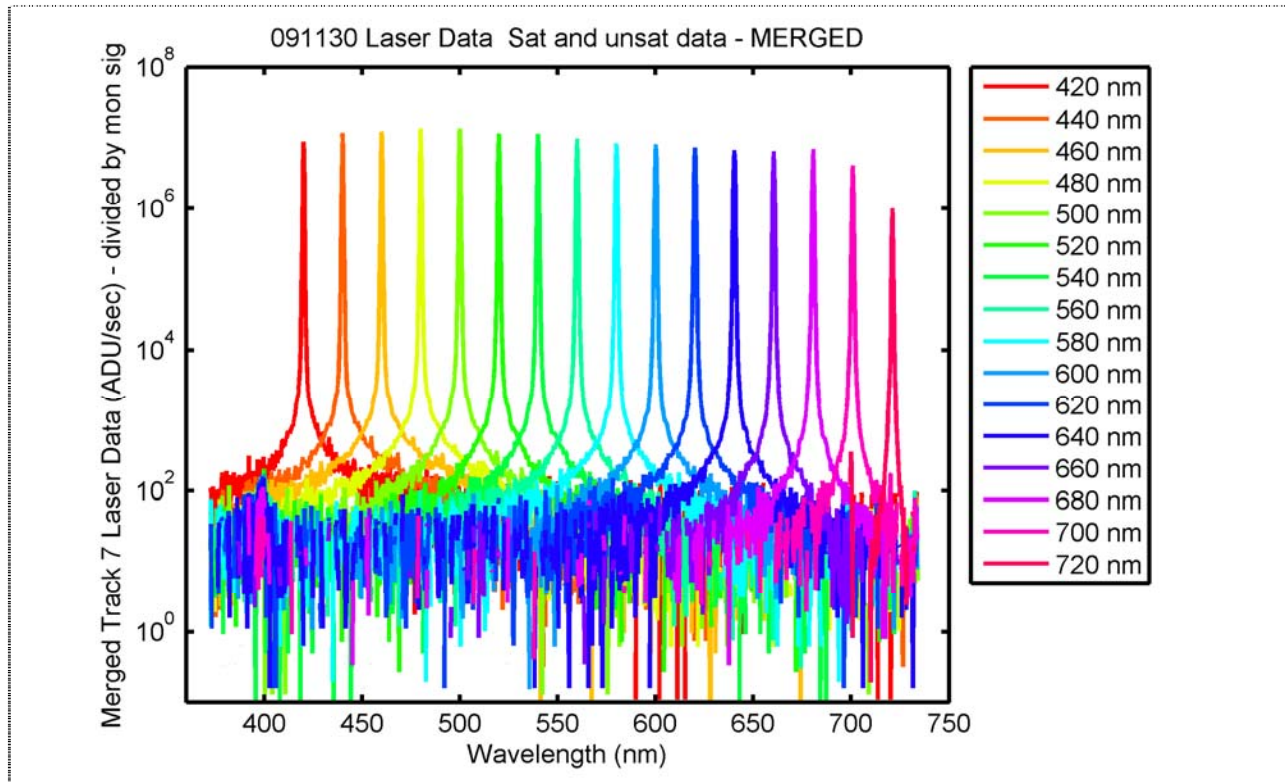


Figure 7. The outputs from 16 different laser inputs for Track 7. The horizontal axis is wavelength and the vertical axis is the average output of the CCD row pixels for Track 7, normalized by the integration time and signal from a monitor photodiode.

The data in Fig. 7 were obtained by combining two different laser scans, one in which the CCD is saturated within the peak in order to get a good signal in the wings and another with the peak unsaturated so as to obtain the correct peak values. This result shows that the observation made from the data shown in Fig. 6 for at a single laser illumination wavelength holds well across the entire spectral region.

For proper interpretation of the data in this multi-channel, hyperspectral spectrograph, the image quality in both the along track (wavelength or CCD column coordinate) and across track (slit height, track, or CCD row coordinate) must be quantified. The lens aberration effect that distorts the image of a single spectral feature as a function of track is called “smile” and the lens aberration effect that distorts the image of a single track as a function of wavelength is called “keystone.” The smile performance was assessed using the wavelength calibration data that was acquired using Hg and Kr spectral line emission lamps for all 14 tracks. Good imaging of these

spectral features is when the bandpass and line center are the same for all tracks. Smile distortion is when the line center is a function of across track position in a symmetric fashion about the center of the CCD. Resonon predicted the maximum smile distortion to be about 0.25 pixel in the middle of the spectral range and about 0.5 pixel at the upper and lower limits of the spectral range for both the blue and the red spectrographs. The two spectrographs exhibit differing amounts of the smile and keystone aberrations because their lens design and fabrication differ slightly. To assess the smile distortion, the observed spectral lines used for the wavelength calibration were fitted to Gaussian profiles and the relative difference of the line centers for the various tracks determined. The results are shown in Tables 2 and 3. These results show that the deviations caused by the smile are less than plus or minus 0.5 pixels, in agreement with that predicted (see Table 2 in Appendix A). This small amount of smile can be accounted for by a separate wavelength calibration of each track. A clear trend in bandpass as a function of track was not readily apparent, although there is a hint that in the blue spectrograph the bandpass decreases with increasing track with the opposite trend possible in the red spectrograph. We report the mean and standard deviation of the full-width half maximum (FWHM) from the fits in Tables 2 and 3. With FWHM on the order of 1 nm and the pixel separation corresponding to 0.35 nm (0.40 nm) for the blue (red) spectrograph, the new system would be comparable to MOBY in bandpass but increases the spectral sampling by about a factor of 2.

Table 2 Wavelength calibration results for the blue spectrograph.

Wavelength (nm)	Maximum difference (pixels)	FWHM (pixels)	FWHM (nm)
404.66	0.30	2.28 ± 0.13	0.82 ± 0.05
546.08	0.19	2.62 ± 0.24	0.95 ± 0.09
690.87	0.34	2.48 ± 0.28	0.90 ± 0.10

Table 3 Wavelength calibration results for the red spectrograph.

Wavelength, nm	Maximum difference (pixels)	FWHM (pixels)	FWHM (nm)
546.08	0.27	2.60 ± 0.16	1.08 ± 0.07
728.73	0.41	2.85 ± 0.70	1.18 ± 0.29
892.87	0.66	2.86 ± 0.27	1.19 ± 0.11

The across track performance was assessed using images of a broadband source, see Fig. 4. During field use, full images such as these will not be routinely available because of limitations of data storage and transmittal. Instead, during the calibration of the instrument, the boundaries for the tracks will be determined, see the horizontal lines in Fig. 5, and the across track average of these defined CCD rows will be reported. To maximize the dynamic range of the instrument, this averaging will be performed in hardware (on-chip binning) as well as software, with the on-chip binning parameters optimized to give the lowest noise for each track. Good imaging in the across track dimension means, among other things, that the track boundaries are independent of along track (wavelength) coordinate. Keystone distortion, which like smile is symmetrical about the optical axis, results in tracks that are not “level,” see Figs. 4 and 5. In Figs. 8 and 9, the variation in signal in the across track dimension for selected wavelengths is illustrated for an edge and center track for the blue spectrograph illuminated by a broadband source. The various

colored lines plotted represent different wavelengths and the dashed black line indicates the peak location on the lower side of the track at the different wavelengths. The output signal varies with wavelength because the source output and the instrument sensitivity vary spectrally. Keystone distortion is a clearly evident for Track 2 (Fig. 8) but it is negligible for Track 8 (Fig. 9). The optical design by Resonon was not optimized to reduce keystone distortion, although the company has experience in building instruments that do not exhibit this effect. This issue would be addressed in any follow-on optical design.

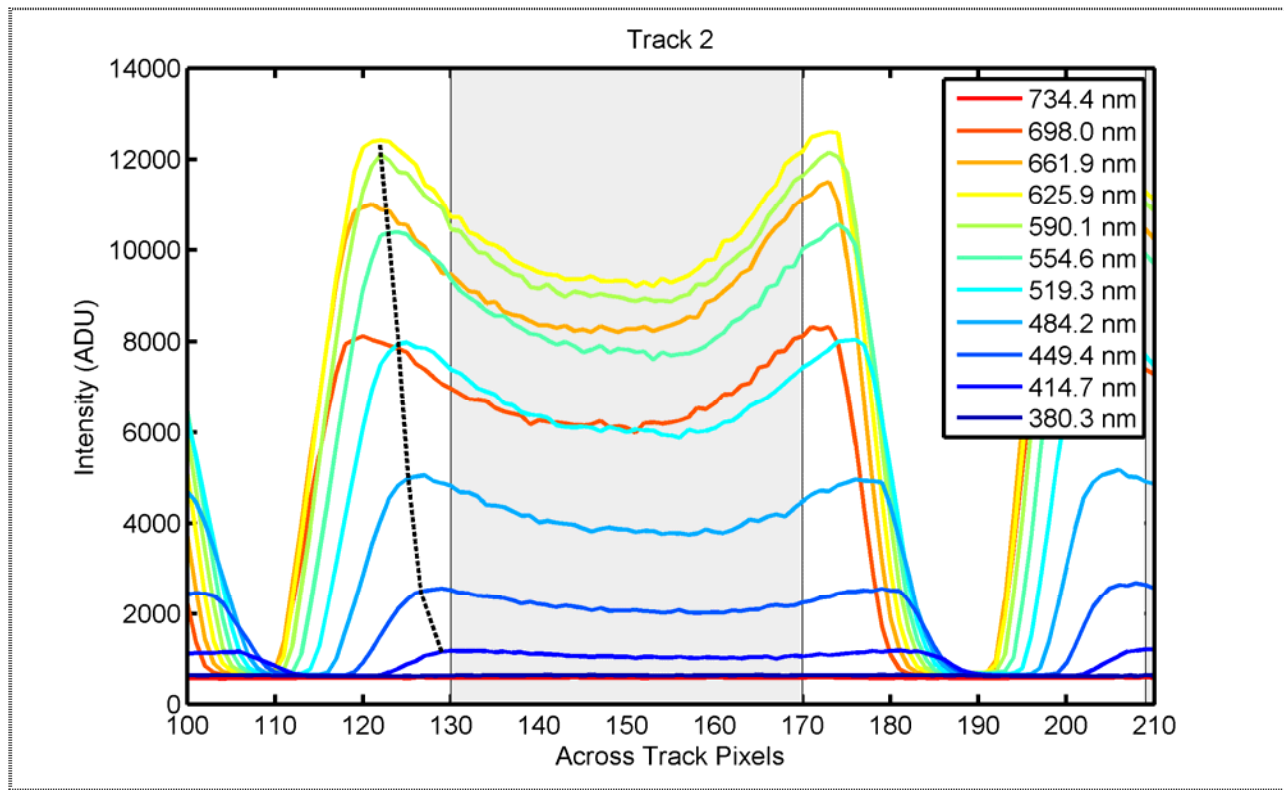


Figure 8. Keystone distortion for Track 2 of the blue spectrograph. The horizontal axis is the CCD row pixel across the track (vertical coordinate in Fig. 4) and the vertical axis is the output in ADU. Track 2 is defined from pixel 130 to 170 (gray region). Eleven profiles are illustrated, corresponding to different wavelengths (see legend).

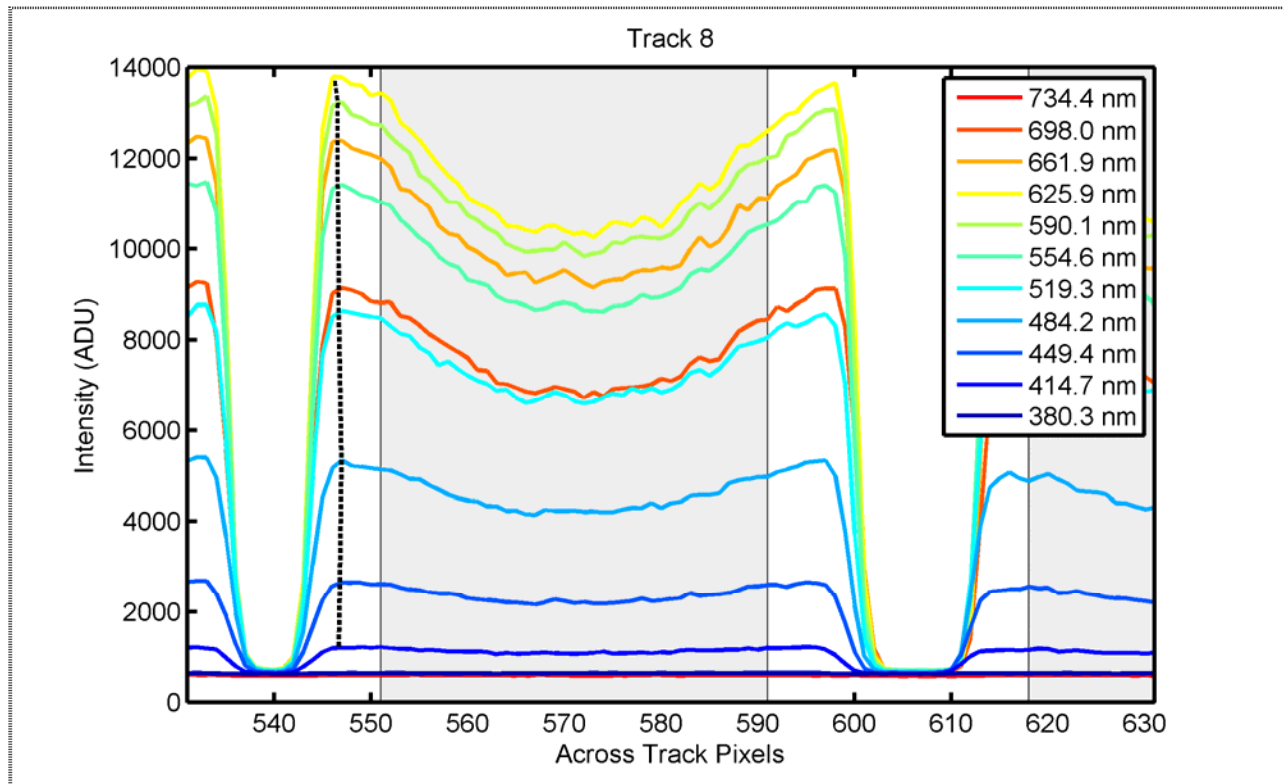


Figure 9. Keystone distortion for Track 8 of the blue spectrograph. The horizontal axis is the CCD column pixel across the track (vertical coordinate in Fig. 4) and the vertical axis is the output in ADU. Track 8 is defined from pixel 551 to 591 (gray lines). Eleven profiles are illustrated, corresponding to different wavelengths (see legend).

The reason for the trough shape of these images is not fully understood at this time but is most likely due to the shape of the distribution of the light from the fiber optics coupled to the slit as well as possible diffraction effects. This is an area of continued pursuit in order to better understand the image shape and fully characterize the spectrograph. For many reasons including aberrations, diffraction and possible other effects, the images in spectrograph focal planes are often complex. What is important for their use however is that they remain stable with time and use so that the instrument can be reliably calibrated. We have done some preliminary work of assessing the stability of the instrument output by varying the width of the shaded area used for summing and found little change as long as one avoids the edges of the tracks.

It is good to see that the signal goes to nearly the background offset in the region between the tracks which means there is minimal cross talk between the channels. In the present utilization as shown in Figs. 8 and 9, there are about 40 pixels (Track 2) and 25 pixels (Track 8) between the tracks which are not used to avoid edge effects and the steep portions of the curves where some minor image shift could cause significant signal change. A detailed study of the cross talk was not possible, but the initial results are promising, see Fig. 10. Here we compare the Resonon to the KOSI Holospec by examining the results on an unilluminated track adjacent to an illuminated track. In the spectral regions where there is adequate signal, the cross track effect in the Resonon is half that in the Holospec.

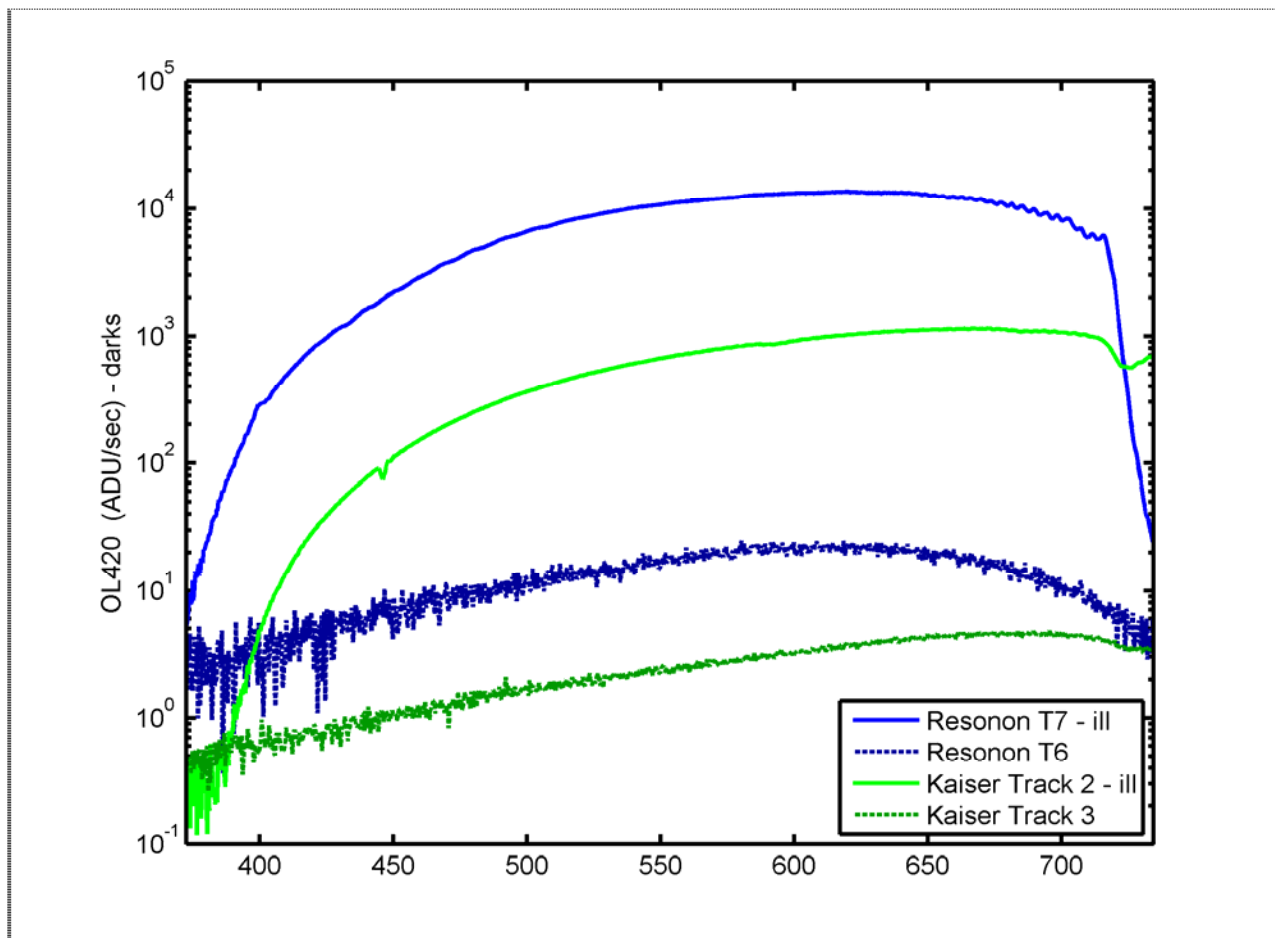


Figure 10. Cross track results for the blue Resonon spectrograph and the KOSI Holospec spectrograph. For this test, one track was illuminated with a white light source (results shown as solid lines) and the results on an adjacent track examined (dashed lines).

As mentioned above, there was not time for a full stray light correction for all 14 tracks. The SIRCUS data for Track 7 was adequate to develop a preliminary stray light correction matrix, apply the correction, and validate the results by looking at the output of some known calibrated light sources. These results are shown in Figure 11 below. This figure illustrates the calibrated levels for an Optronic Laboratories, Inc. (OL) sphere source with various filters as specified in the legend inserted between the external lamp and the sphere. It was measured by the blue spectrograph on Track 7 and the results are shown in Fig. 12. The Resonon instrument gives a distorted measurement in the region beyond 750 nm because of a 720 nm low-pass filter employed in the instrument.

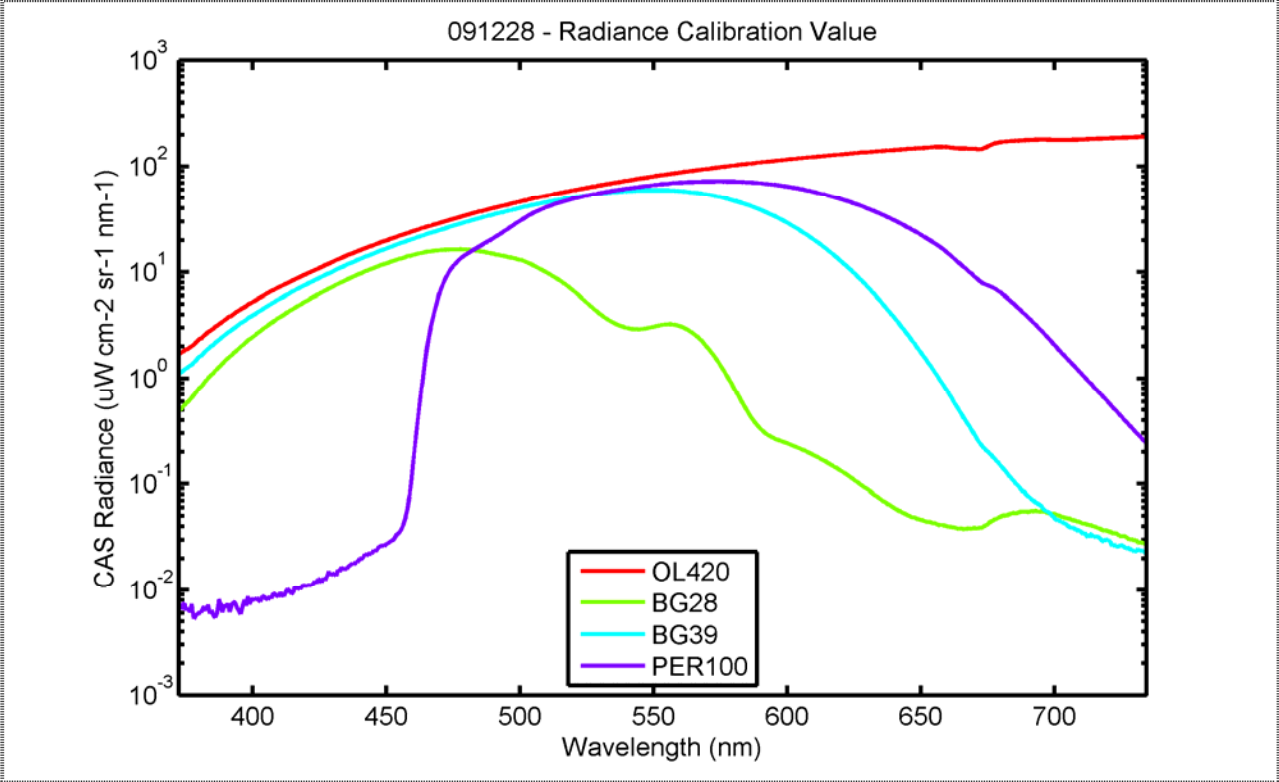


Figure 11. Radiance levels for four calibrated sources. The sources were an OL model 420 integrating sphere source with various filter combinations to generate the unfiltered output as well as those labeled BG28, BG39, and PER100.

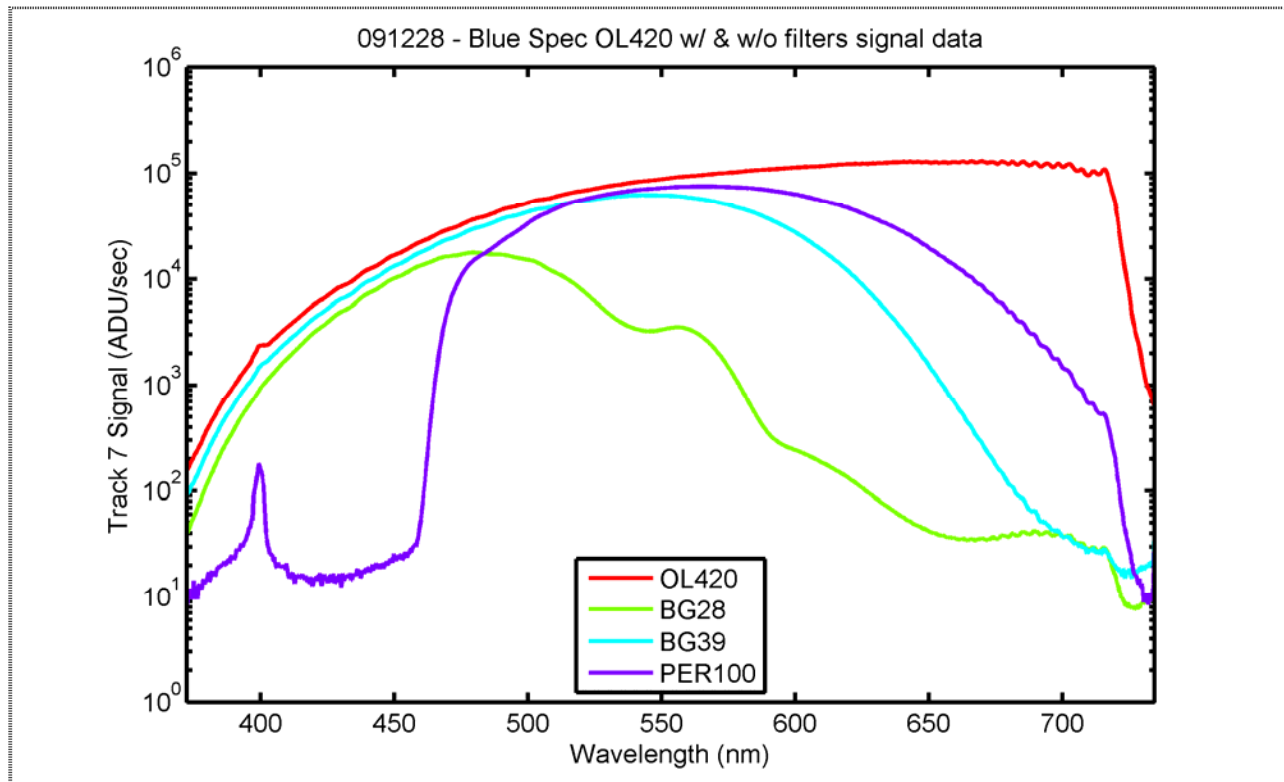


Figure 12. The output of the blue spectrograph on Track 7 for the four sources illustrated in Fig. 11. The vertical axis is in ADU/sec and the horizontal axis is wavelength. The ADU is analog digital units and corresponds to the output of the A/D unit that is part of the CCD electronics. The output for Track 7 has been averaged across track as described earlier. The feature at 400 nm for the PER100 is the zero-order reentry artifact seen in Fig. 5.

The ratio between the calibrated source radiances and the measured signal gives the system response for this track and should be a constant for all four sources. This quick technique gives insight into the performance of the instrument, highlighting areas which need additional consideration. These system response results are shown in Figure 13.

Over the central region of the spectra from 450 nm to 700 nm the results are remarkably similar as they should be. Above 750 nm the deduced system responses do not agree and this region corresponds to the spectral region where the cut-off filter is effective. This can be seen in Fig. 12 where the signal dies off rapidly even though the source spectra indicate significant output, see Fig. 11. It is more difficult to characterize and correct the instrument for stray light in regions of low signal and the measurement uncertainty will increase as well. Once the stray light performance is more thoroughly characterized, the small signal measurements will undoubtedly improve. The signal is also small on the short wavelength side below 450 nm. The behavior of the PER100 source around 460 nm and the overall disagreement in system response below 450 nm is pathological and not well understood at this time. The problem is probably related to the sharp cutoff in the source output, the resulting small signal, the sensitivity to the dark (shuttered) output, or the incompleteness of the stray light correction data. The results for the other sources are consistent in this region and hence there is also the possibility this particular

data set has some error which renders it not usable in the short wavelength region. The origin of the peak near 400 nm in the PER100 and unfiltered measurements by the blue spectrograph on Track 7 is the artifact image mentioned in Fig. 5.

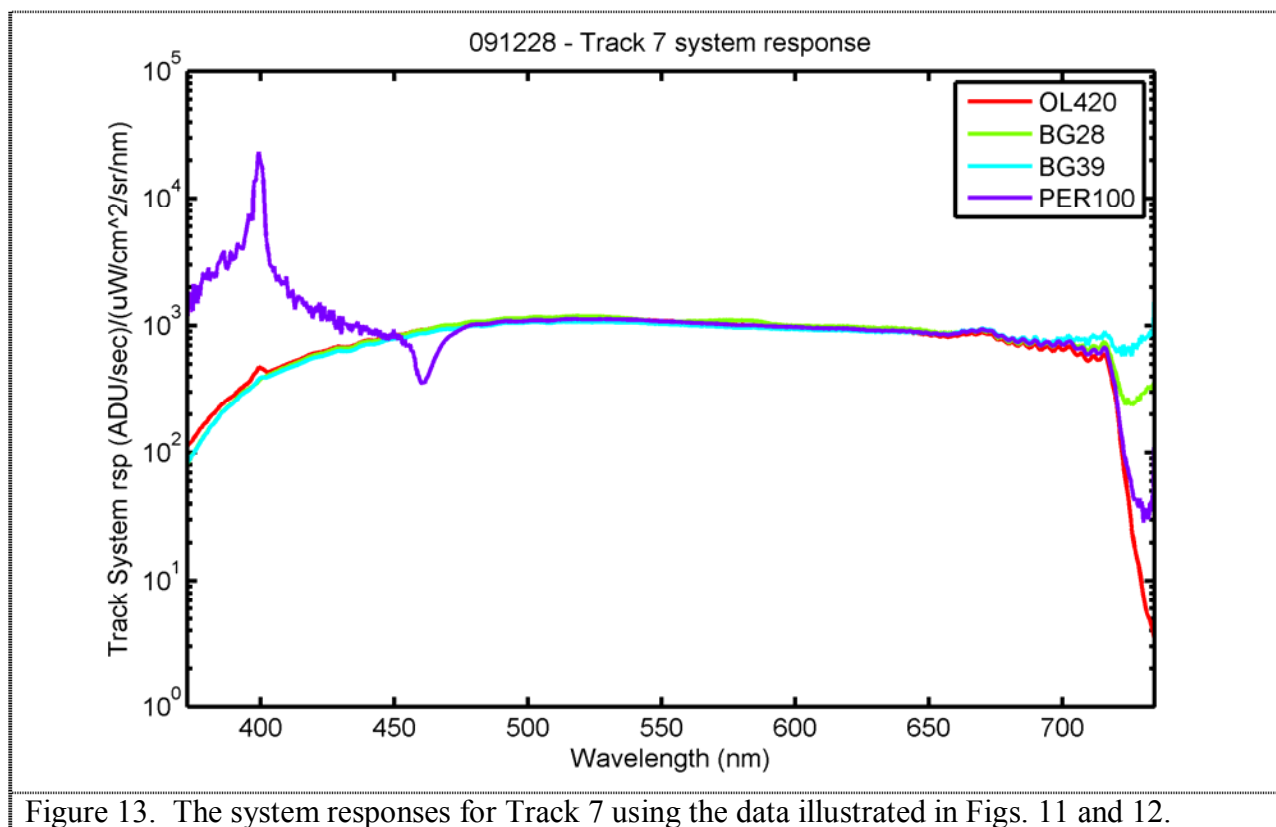


Figure 13. The system responses for Track 7 using the data illustrated in Figs. 11 and 12.

Conclusions and Summary

The instruments performed according to specification and in fact the apparent stray light rejection appears to be the best of any CCD array device recently tested by NIST. The low scattered light in the system coupled with its high responsivity and radiometric performance of the camera makes this instrument a viable choice as the sensor in a hyperspectral multichannel ocean color system. We recommend the design to function as the spectrograph system for a new MOBY instrument. The team involved believes this new instrument study has been highly successful and that the spectrograph performance has met or exceeded expectations and performance requirements.

The work is continuing at NIST with MLML under the one year NOAA funding. We plan to continue to develop the instruments; this includes replacing the 1 m long input fibers with a short assembly that couples from the slit to an optical interface assembly that has individual shutters for each channel. The blue and the red spectrograph will be packaged for shipboard deployment, with 7 long input fibers coupled to sample in-water collectors such as those described in Yarbrough *et al.* (2007). Data acquisition software will be developed, selected characterizations will be performed, optical collectors installed, and calibrations implemented. A limited set of

field data is planned in attended, real time operating mode with wireless communication. In addition, we wish to address the saddle shape in the across track profiles, and we need to address the blue artifact in the blue Resonon spectrograph. Our recommendation is to replace the PGP element at this time, because we feel the additional measurements at SIRCUS that would be necessary to implement this correction will be difficult because we need very high laser power levels to model the feature accurately. The cost of the new PGP element is commensurate with the costs of the additional laboratory and analysis effort necessary to implement the correction, and testing the new PGP is a risk reduction step for full scale development of this design.

Acknowledgments

Many people have contributed to this effort and we are grateful to them all – Mark Yarbrough, Mike Feinholz, and Stephanie Flora of MLML; Mike Kehoe, Casey Dodge, and Rand Swanson at Resonon; Al Parr, Bob Saunders, Steve Brown and Zhigang Li at NIST; and Dennis Clark of Marine Optical Consulting. Useful discussions have been held with Ken Voss at the University of Miami and Eric Shirley at NIST.

References

- Brown, S.W., G.P. Eppeldauer, and K.R. Lykke (2006). “Facility for spectral irradiance and radiance responsivity calibrations using uniform sources.” *Appl. Optics* **45**, 8218-8237.
- Clark, D.K., M.A. Yarbrough, M. Feinholz, S. Flora, W. Broenkow, Y.S. Kim, B.C. Johnson, S.W. Brown, M. Yuen, and J.L. Mueller (2003). “MOBY, a radiometric buoy for performance monitoring and vicarious calibration of satellite ocean color sensors: measurement and data analysis protocols,” in *Ocean Optics Protocols for Satellite Ocean Color Sensor Validation, Revision 4, Volume 6*, J.L. Mueller, G.S. Fargion, and C.R. McClain, Eds., NASA Goddard Space Flight Center, Greenbelt, MD. p. 3-34.
- Feinholz, M.E., S.J. Flora, M.A. Yarbrough, K.R. Lykke, S.W. Brown, B.C. Johnson, and D.K. Clark (2009). “Stray light characterization of the Marine Optical System.” *J. Atmos. Oceanic Technol.* **26**, 57-73.
- Franz, B.A., S.W. Bailey, P.J. Werdell, and C.R. McClain, F.S. (2007). “Sensor-independent approach to vicarious calibration of satellite ocean color radiometry,” *Appl. Opt.* **46**, 5608-5802.
- Kehoe, M. and C. Dodge (2009). *Report on Blue and Red Imaging Spectrometers for MOBY*, Internal Report, Resonon, Bozeman, Montana, 16 pp.
- Yarbrough, M.A., S. Flora, M.E. Feinholz, T. Houlihan, Y.S. Kim, S.W. Brown, B.C. Johnson, K. Voss and D.K. Clark (2007). “Simultaneous measurement of up-welling spectral radiance using a fiber-coupled CCD spectrograph.” *Proc. SPIE* **6680**, 66800J-1 to 66800J-11.
- Zong, Y., S.W. Brown, B.C. Johnson, K.R. Lykke, and Y. Ohno (2006). “Simple spectral stray light correction method for array spectroradiometers.” *Appl. Optics* **45**, 1111-1119.

Appendix A
Adapted from:
Report on Blue and Red Imaging Spectrometers for MOBY
April 2009
Michael Kehoe and Casey Dodge
Resonon, Inc., Bozeman, MT

The redesign of the NIST Blue and Red imaging spectrometers is now complete. This document describes the results of this effort. The report is divided into three sections, the first dealing with the mechanical design, the second with the optical design, and the third with summary remarks.

General characteristics of the system are provided in the following table.

<i>Table 1: Key Characteristics of Blue and Red Imaging Spectrometers</i>		
Characteristic	Blue	Red
diameter	3.9" (spectrometer) 5.4" (mounting flange)	3.9" (spectrometer) 5.4" (mounting flange)
length	16.4" (not including connectors or fiber bundle)	17" (not including connectors or fiber bundle)
wavelength range	370-720 nm (optimized from 390-720 nm)	500-900 nm
size of image	13mm x 13 mm	13 mm x 13 mm
silt dimensions	13 mm x 25 μ m	13 mm x 25 μ m
mechanical component material	6061 aluminum	6061 aluminum

The overall layouts of the two systems vary only slightly and will be discussed together as one.

1. Mechanical Design

An external view of the system is depicted in Figure 1. This figure shows a fiber bundle attached to a cylindrical housing containing an imaging spectrometer, which in turn is attached to a camera. The fiber bundle consists of 15 separate fiber optic strands, each of which has an 800 μ m core, mounted in a ferrule made of 316 stainless steel. The fibers are arranged in a line within the ferrule. It will be fabricated by RoMack, Inc. The camera is a Princeton Instruments Pixus 1024, as specified by NIST personnel. The cylindrical outer shell is composed of anodized 6061 Al. The heart of the system is the imaging spectrometer within this casing. It consists of seven integrated assemblies, which are discussed below in turn.



Figure 1: Overview of system.

The fiber bundle attaches to the fiber bundle mount, as illustrated in Figure 2. This module connects the fiber bundle to the imaging spectrometer. A series of silicone O-ring seals in the mount and in a cap that captures the outer shell are used to seal the spectrometer from outside contaminants. The mount, made of anodized aluminum, is designed to allow precise rotational adjustment of the fiber bundle so that it can be aligned with the rest of the imaging spectrometer while maintaining its axial position in the optical train. Once this alignment is done, the mount can be locked securely in position. A curved slit is attached to this unit via a small flexure mount. This flexure allows the slit to be translated perpendicular to the optical axis of the system in order to achieve optimum distortion correction. Once the slit is positioned, this mount also locks down for stability.

The next three assemblies, referred to as the first lens barrel, second lens barrel, and PGP (prism-grating-prism) mount are also illustrated in Figure 2. Both lens barrels are made from anodized aluminum and together they contain the five lenses used to collimate light emerging from the slit. The first lens barrel, containing the first two lens elements, is screwed into the second barrel which also houses the fiber slit assembly and the PGP mount. The first lens barrel's position along the optical axis of the system is adjustable via fine pitch threads and can be locked in place with a threaded ring. The second lens barrel contains the remaining three lens elements of this portion of the system. The prism-grating-prism light dispersion element (PGP) is held in a rotation mount in the end of the second lens barrel opposite the fiber bundle mount. The rotation capability of this mount permits the PGP to be aligned with the slit and detector.

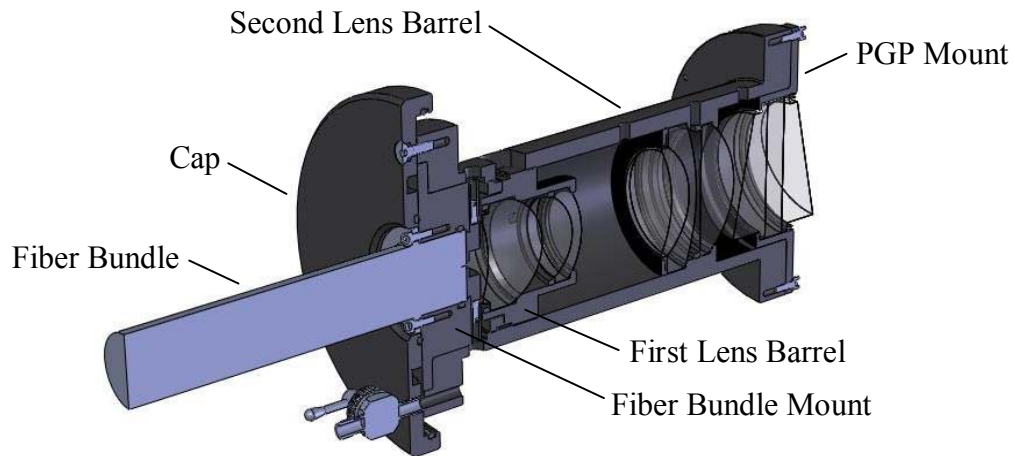


Figure 2: The front portion of the imaging spectrometer.

The third and fourth lens barrels along with the camera mount, illustrated in Figure 3, contain the three lenses used to focus the light coming from the PGP onto the detector. Both barrels and the camera mount are made from anodized aluminum. The fourth barrel is screwed into the camera mount so that it can be translated for final focus adjustment. It is locked in place with a threaded lock ring. An asymmetric baffle is mounted to the end of the third lens barrel and an annular baffle is mounted just before the sixth lens to control stray light. These inserts are made from aluminum and coated with a special ultra-black anodization process. The camera mount is an anodized aluminum flanged tube that connects the third lens barrel to the front face of the camera adapter. A silicone o-ring seals the interface between the camera mount and the camera adapter and another forms a seal between the camera mount and the outer shell. The camera adapter replaces the front plate of the Pixus camera in order to seal the system more effectively. It includes a flange for mounting the entire system and sets the spacing between the final lens of the spectrometer and the image plane of the camera. An o-ring seals the interface between the camera and the camera adapter. This adapter may be replaced in order to attach a different camera to the system. As depicted in Figure 3, the entire imaging spectrometer is offset from the detector's optical axis, a feature dictated by optical requirements of the system.

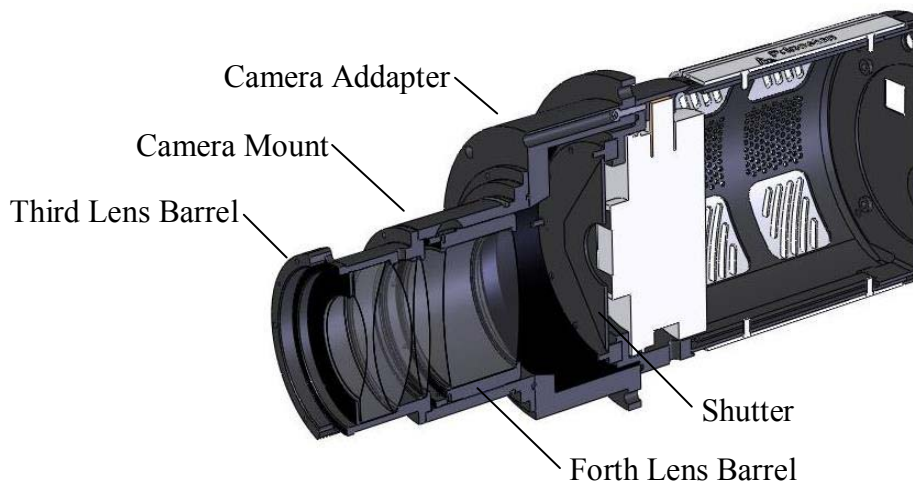


Figure 3: The back portion of the imaging spectrometer.

Throughout the system, all internal faces that are not threaded or mating surfaces will be painted with an optically black paint or coated with the Avian DS black batch process to reduce stray light. All fasteners are made from 316 stainless steel to minimize corrosion due to possible exposure to salt water. Air cavities have been vented to allow purging with nitrogen. A valve has also been incorporated for this reason. A humidity indicator with light sealing cap provides a means of monitoring the humidity inside the instrument. Two internal thermistors, one near the slit and one near the grating, together with one external thermistor near the camera are also provided to measure temperatures at these points.

2. Optical Design

The optical redesign was conducted with an eye towards reducing costs from those of the original Blue and Red systems. The primary means used to accomplish this end is identical optical components in both systems. This allows for scale economies in optical component fabrication, which tend to be large. Figure 4 illustrates the optical components of the two systems. Each system consists of nine lenses, two prisms and a transmission grating. Eight of the nine lenses are identical in both systems, excepting the anti-reflection coatings. The systems are customized to different wavelength ranges by means of the non-identical lens element, the prisms, the gratings, and the component spacings.

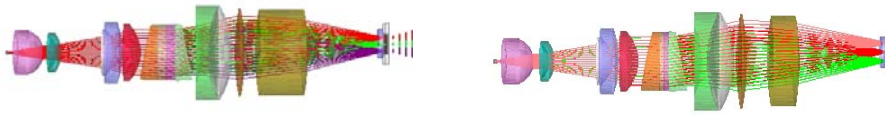


Figure 4: Blue system (left) and Red system (right). All elements except the prisms, gratings and the last (rightmost) lens are identical.

The revised Red and Blue systems both make use of design features utilized in the original Blue system. A curved slit is used to correct grating distortion (i.e., smile) and image quality in the spatial dimension is permitted to be much lower than it is in the spectral dimension. These features permit the systems to achieve performance targets with a reduced set of lenses. Optical performance of the Blue and Red systems are characterized in terms of quality of the signal and quantity of the noise. These two performance criteria are discussed in the next two subsections.

2a. Quality of the Signal

Key performance parameters for the two systems are provided in Table 2. Summary findings on optical performance are as follows: 1) single pixel spectral resolution from 390 to 720 nm for the Blue system and from 500 to 875 nm for the Red system, 2) worst case smile distortion less than 1/2 pixel for both systems 3) efficiency in excess of 50 percent from 370 to 580 nm for the Blue system and from 525 to 875 nm for the Red system, 4) variation in performance resulting from moderate temperature changes, i.e., $20^\circ \pm 15^\circ$ C immaterial for the Blue system and moderate for the Red system.

Table 2: Key Optical Performance Parameters	
Blue System	
Mid-Field Spectral MTF @ 38 lpmm (%)	
390 nm	47
545 nm	76
700 nm	70
Maximum Smile Distortion	
390 nm	~ 1/2 pixel
545 nm	~ 1/4 pixel
700 nm	~ 1/2 pixel
Efficiency (%)	
370 nm	61
430 nm (peak)	73
720 nm	20
Maximum Thermal Drift	
20° C to 5° C	< 1/4 pixel
20° C to 35° C	< 1/4 pixel
Red System	
Mid-Field Spectral MTF @ 38 lpmm (%)	
500 nm	72
700 nm	61

900 nm	46
	Maximum Smile Distortion
500 nm	~ 1/2 pixel
700 nm	~ 1/4 pixel
900 nm	~ 1/2 pixel
	Efficiency (%)
500 nm	48
660 nm (peak)	74
900 nm	48
	Maximum Thermal Drift
20° C to 5° C	< 1/3 pixel
20° C to 35° C	< 1/3 pixel

Spectral resolution - Blue System: Resolution is readily measured in terms of the modulation transfer function (MTF). MTF data for the Blue system at the center temperature (20° C) and at 390, 545 and 700 nm wavelengths is provided in Figure 5. Both sagittal and tangential MTF data is shown, representing both the spatial (sagittal) and spectral (tangential) dimensions.

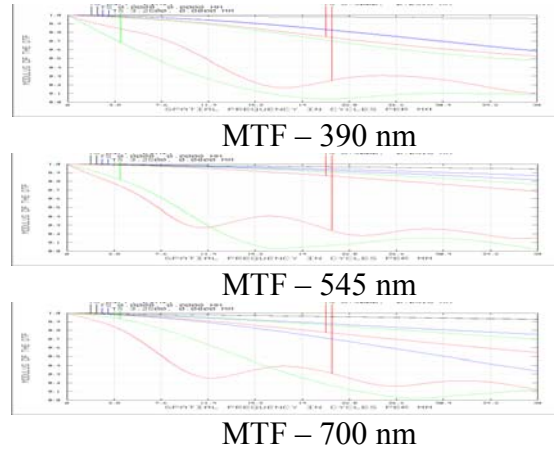


Figure 5: MTFs for the Blue system.

The blue lines represent the performance at the center of the slit, the red lines represent the top (and bottom) of the slit, and the green lines represent the midpoint between these two. The Nyquist frequency for the camera is 38 lines per mm. At this frequency, the MTF is in excess of 40 percent at all fields and at all wavelengths over 390 nm in the spectral (tangential) dimension. Since 40% modulation is certainly resolvable and, according to Warren Smith, one line pair per dimension satisfies the criterion of being detectable, the instrument provides single pixel spectral resolution under this criterion. Resolution drops off sharply below 390 nm, providing roughly 3-pixel resolution at 370 nm.

It is clear from the MTF data that resolution in the spatial dimension is poor at all wavelengths and off-axis fields. This occurs because almost all of the available degrees of freedom are used to correct for aberrations in the spectral direction, and the system is on-axis in this direction. Spatial resolution should be just good enough to prevent cross talk between fiber channels.

The actual performance will be somewhat lower than the figures shown in Figure 5 owing to manufacturing and alignment tolerances, but we anticipate these losses to be small.

Spectral resolution - Red System: See Appendix 1 for MTF data for the Red system.

Distortion: The predominant concern regarding distortion is spectral “smile” distortion. Smile is measured for a given wavelength as the curvature (i.e., smile) of the spectral line on the image plane. Planar diffraction gratings, such as the one used in this project, all generate smile distortion to some extent. The primary means of correcting for it in this system is a curved entrance slit. The slit is curved in a manner diametrically opposite to the distortion generated by a grating in conjunction with a straight slit, resulting in a straight-line image of the slit on the image plane. Exact curvature specifications were numerically optimized in Zemax. The

resulting slit is 13 mm in length, 25 μm in width, and deviates from a straight line over its length by 50-60 microns for each system.

In order to describe how smile distortion is measured, define x and y coordinates on the CCD as follows: x = spatial dimension; y = spectral dimension. Assuming the origin is at the center of the CCD, x extends from -6.5 mm to 6.5 mm and y extends from -6.5 mm to 6.5 mm on the CCD. According to Zemax models, worst case smile distortion occurs at 720 nm at full slit height for the Blue system. In this case, the axial coordinate value on the CCD is (0, 6.500) and the coordinate value at the top of the field (corresponding to the top of the slit) is (6.5, 6.494). Smile is measured as the y-distance between these two coordinates, which amounts to .006 mm. A similar worst-case value for smile distortion in the Red system occurs at 900 nm, and the corresponding value is .006 mm.

Efficiency: Transmission is driven by three factors: 1) efficiency of the grating, 2) internal transmission of the lenses, and 3) surface transmission of the lenses. The first two factors are strongly wavelength dependent, while the last is only weakly so in the target spectral range. These factors are discussed in sequence below.

Table 3: System Throughput at Selected Wavelengths				
Wavelength	Grating Efficiency Losses (%)	Internal Transmission Losses (%)	Surface Transmission Losses (%)	Total Throughput (%)
Blue System				
370 nm	19.0	12.1	13.3	62.5
390 nm	14.0	5.8	13.3	70.2
430 nm	11.0	4.2	13.3	74.8
720 nm	76.0	1.8	13.3	20.7
Red System				
500 nm	43.0	2.9	11.8	48.8
700 nm	16.0	2.1	11.8	72.5
900 nm	44.0	1.9	11.8	48.4

Wasatch Photonics and Kaiser Optical, the companies designated to manufacture the Blue and Red gratings, respectively, have provided us with plots of their estimates of grating efficiency over the 370-720 nm range and 500-900 nm wavelength ranges. Estimated grating efficiency ranges from 24 to 89 percent for the Blue system and 56 to 86 percent for the Red system.

Internal transmittance losses are large in the near ultraviolet and moderate elsewhere. Losses of this type peak at 12% for the blue system at 370 nm. Surface transmission losses are estimated to be 0.6% per surface for the blue system and 0.5% for the Red, with little wavelength

dependence. One surface of one element is coated with a filter that blocks wavelengths greater than 720 nm for the Blue system and less than 500 nm for the Red system. This surface also reflects around 4% of the within-range radiation.

Total transmission, or efficiency, is the product of the percentage throughput from the three factors identified in Table 3. It ranges from 20 to 75 percent for the Blue system and from 48 to 75 percent for the Red system.

Thermal Issues: The optical glasses and the substrate material were chosen to obtain reasonable thermal stability over the 0 to 40 °C range. Zemax computations indicate that a substrate material with a CTE somewhat above 30 (E-6/°C) would provide optimal thermal stability. The high CTE value is driven by a couple of lenses composed of material with high negative values of the temperature coefficient of refractive index. Aluminum 6061, with a CTE of 23.6, provides satisfactory thermal stability and is deemed to be the best choice of substrate material for the purpose at hand. The systems were thermally stabilized at 5°, 20°, and 35° C. The endpoints of the target temperature range were not used for stabilization purposes to avoid overweighting them.

Two metrics were identified for characterizing thermal stability. The first is thermal drift, or the change in the position on the CCD associated with a given wavelength resulting from a change in temperature. The primary means for controlling thermal drift is the glass choices for the three elements of the PGP. After a careful search, Ultran30 was identified as the best choice for the Blue system and S-NBM51 for the Red system. The former is an unusual glass, but it is currently available. N-BK7 was identified as the best choice of glass for the grating in both systems. For the Blue system, the resulting thermal drift is less than 1/4 pixel for a temperature change of ± 15 °C from the central temperature of 20 °C. For the Red system, the drift is less than 1/3 pixel for a comparable change in temperature.

Table 4: MTFs at Different Temperatures*

Blue System			
wavelength (nm)	390	545	700
5 °C	49	75	71
20 °C	47	76	70
35 °C	46	77	69
Red system			
	500	700	900
5 °C	72	56	50
20 °C	72	61	46
35 °C	72	64	42
*Measured as a percentage. All data values are for mid-field at 38 lpmm.			

The second metric for characterizing thermal stability is the change in MTF performance with temperature. This change is small and hence is more readily explained numerically than graphically. Table 4 provides MTF values for three wavelengths and temperatures. It is clear

that the variation in spectral resolution with temperature is a minor issue for either system.

2b. Stray Light

Stray light analysis was performed using FRED optical engineering software. The optical components that were modeled consist of the lenses, prisms and grating, plus the camera cover window and detector. The hardware components that were modeled consist of the lens barrels, lens mounts, and interior baffles. All refractive components are modelled as having AR coatings; all metallic surfaces are either black anodized or coated with Avian DS Black, a highly light absorbent anodization process.

Stray light can be separated into two categories, one encompassing ghost reflections off refractive surfaces and the other encompassing various types of scattering. Ghost reflections are discussed first, followed by a discussion of scattering and several related topics.

Ghost Reflections: The chief source of stay light incident upon the detector is from ghost reflections off of the system's refractive optical elements. All stray light of this form that reaches the detector involves an even number of reflective "bounces" off of these components. Since all refractive surfaces in the system are AR coated with less than 1% reflectivity, the strength of the ghost beam drops off precipitously with each additional reflection, so that only double-bounce reflections materially affect system performance. Moreover, as will be seen, double-bounce ghost reflections involving a first "bounce" off of the detector constitute the predominant stray light problem.

Before specific ghost pathways can be analyzed, the reflectivities of the surfaces off which the ghosting occurs must be specified. The specifications used in this analysis are provided in Table 5:

	Blue System		
	440 nm	560 nm	680 nm
refractive elements	.006	.006	.006
detector	.17	.16	.23
	Red System		
	500 nm	700 nm	900 nm
refractive elements	.005	.005	.005
detector	.34	.08	.24

Light incident upon the detector and not registered as a "good" signal is either reflected, scattered, or absorbed. Based on fragmentary reflectance data reported by detector manufacturers and direct examination of the detector surface, it appears that majority of this unregistered light is specularly reflected from the surface of the detector. Little appears to be known about how much light is scattered by the detector, but visual examination of the detector

surface suggests it is not large. With these points in mind, we have assumed that the amount of specular reflection off the detector surface is described by the equation:

$$\text{specular reflection} = 1 - \text{quantum efficiency} - .02,$$

where quantum efficiency is for the Pixis 1024 detector with a broadband coating. The 2 percent value in the equation represents light that is scattered or absorbed by the detector.

Table 6 provides a listing of the worst double-bounce reflections in the Blue system and Table 7 provides similar data for the Red system. Not surprisingly, the worst ghost reflections in both systems involve a reflection off of the detector followed by a reflection off one of the surfaces of the fused silica window immediately in front of it. There is nothing that can be done about this type of ghost reflection, other than removing the window. These reflections account for over 1/3 of total ghost power on the detector.

			Power at Detector (power entering at slit \equiv 1)		
1st Reflective Surface	2nd Reflective Surface	Distance From Focus to DMD (mm)	420 nm	540 nm	660 nm
CCD surface	detector window, either surface	3-7	.0007	.0005	.0003
CCD surface	lens 1, surf 1	22	.0003	.0001	.0000
CCD surface	lens 9, surf 1	42	.0004	.0001	.0000
CCD surface	doublet 1, surf 2	25	.0001	.0001	.0000
Total double-bounce ghost power (percentage of "good" radiation on detector at given wavelength)			.0033 (.51%)	.0017 (.35%)	.0009 (.34%)

			Power at Detector (power entering at slit \equiv 1)		
1st Reflective Surface	2nd Reflective Surface	Focus Distance	520 nm	700 nm	880 nm
CCD surface	detector window, either surface	3-7	.0006	.0003	.0003
CCD surface	lens 1, surf 1	22	.0001	.0001	.0002
CCD surface	doublet 1, surf 2	24	.0001	.0001	.0000
CCD surface	lens 9, surf 1	31	.0003	.0000	.0000
Total double-bounce ghost power (percentage of "good" radiation on detector at given wavelength)			.0021 (.56%)	.0014 (.20%)	.0009 (.23%)

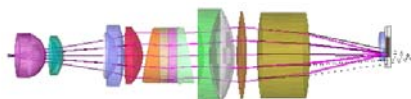


Figure 7: Ghost image from ghost reflection off of detector and last lens, Blue system. The whole path is: slit \rightarrow detector \rightarrow lens 9 surface 1 \rightarrow detector. The pink rays depict the path from the detector to lens 9 surface 1. The black rays depict the path from lens 9 surface 1 to the detector.

Only one other surface in the back end optics has a ghost reflection of material importance. This

ghost involves the first surface of the Lens 9, and it is depicted for the Blue system in Figure 7. The optics upstream from the grating contain several surfaces that reflect material amounts of stray radiation onto the detector. An illustration of one of the worst offenders is provided in Figure 8, which shows the last segment of the following light path: slit → detector → lens 1 surface 1 → detector. In all cases, ghost images were mitigated by adding lines to the Zemax merit function to push the focal point of radiation along these pathways away from the detector.

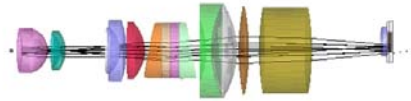


Figure 8: The last segment of the optical path: slit → detector → lens 1 surface 1 → detector, Blue system. Only the path from surface 1 of lens 1 to the detector is illustrated.

According to the data in Tables 7 & 8, the aggregate amount of stray light power on the detector from double-bounce ghost reflections is .3% - .5% of the "good" signal on the detector for the Blue system. The comparative number for the Red system is about .2% - .6%. In both cases, stray light performance will be worse towards the bottom of the wavelength range because this area of the detector is situated close to optical axis where stray light tends to concentrate. The generally better performance for the Red system is attributed mainly to the better performance of the AR coatings, which in turn occurs because of the narrower wavelength band, measured in octaves.

Scattering and Miscellaneous: The second stray light category is scattering, by which we mean stray light other than specular ghost reflections. This type of stray light stems from residual reflections off of black coated surfaces, dust and imperfections on refractive surfaces, various types of scattering within refractive materials, and non-specular reflections off of the detector. Only scattering off of black surfaces and the detector will be considered here. Assumptions on the scattering properties of the affected surfaces are as follows:

Table 8: Scattering Specifications for Black Surfaces, Lens Edges, and the Detector

	Type of Scattering	Total Integrated Scatter
black anodization	BRDF for black paint from FRED	5%
Avian DS black anodization	BRDF for black paint from FRED	0.7%
Rough Ground Glass	Lambertian	50%
Detector	Lambertian	0% or 1%

The reflectivity values for both types of black anodization are taken from Avian Technologies data, while those of rough ground glass and the detector are ad hoc estimates. The results that follow indicate that scattering from rough ground glass is immaterial, so little more needs to be said about it. Scattering from the detector also appears to be of minor importance.

Results of the scatter analysis are provided in Table 9. The first two rows show results for stray light associated with the primary beam, which reaches the detector after 1st order diffraction off of the grating. Comparing the results in the two rows, it is clear that scattering off of the detector is responsible for most scatter-variety stray light. Even with detector scattering included, however, the aggregate impact of scattering-induced stray light is an order of magnitude less than that associated with ghost reflections.

Table 9: Scattering and Miscellaneous Stray Light Issues

scattering surfaces	diffraction order	power on detector as % of “good” signal at the given wavelength		
		420 nm	540 nm	660 nm
black surfaces	1	.0002%	.0002%	.0004%
black surfaces & detector	1	.02%	.02%	.02%
black surfaces & detector	2	.000%	.000%	.000%
black surfaces & detector	0	.000%	.000%	.000%
double-bounce ghosts	2	.000%	.000%	.000%
double-bounce ghosts	0	.002%	.003%	.004%
double-bounce ghosts – low f/#r	1	.46%	.33%	.33%

Stray light associated with various other optical pathways are also provided in Table 9. Some conclusions regarding these results are as follows:

- Scattering associated with 0th and 2nd order diffraction: There are potential scattering problems associated with light diffracted by the grating into unused diffraction orders. In particular, the 2nd and higher order diffracted beams crash into the sidewalls and scatter.

To the extent this radiation reaches the detector, it constitutes a stray light problem. Numerical estimates, however, indicate that this problem is immaterial.

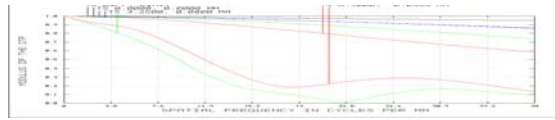
- Double-bounce ghost images associated with 0th and 2nd order diffraction: The significance of these problems is a couple orders of magnitude less than that of 1st order ghost images and hence they can be ignored.
- Effects of NA-increasing stresses to the fiber optics: NIST personnel have pointed out that stress on the fused silica input fibers can increase their NA (decrease $f/\#$). To see if this affects stray light, the system was remodeled assuming an $f/\#$ of 1.8 rather than 2.2 for the input fibers. The double-bounce ghost reflection results are reported in the last row of Table 9.

The above estimates are only as good as the reflectivity assumptions associated with them. In particular, the reflectivity of the detector is crucial to the accuracy of the analysis, and its value has been inferred from quantum efficiency data for the Pixis 1024 detector and fragmentary reflectance data associated with other detectors. To the extent the detector reflectivity values provided here are inaccurate; the resulting stray light percentages will change roughly proportionately.

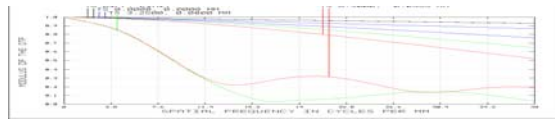
3. Summary

Two imaging spectrometers, one for the 370-720 nm range and the other for the 500-900 nm range, have been designed. Both systems are primarily made from interconnected aluminum 6061 parts. The systems provide pixel limited spatial resolution over most of the wavelength ranges, excepting the edges. They are designed to be thermally stable from 5 to 35 °C, both in terms of spectral resolution and calibration. Various features have been designed into the systems to limit the amount of stray light reaching the detector. The residual stray light that does register on the detector primarily stems from double-bounce ghost reflections. The level of stray light from this source varies from .2% to .6%, depending on the system and position on the detector.

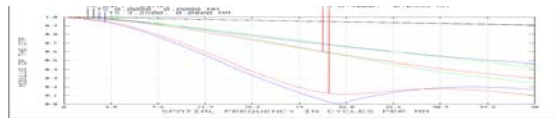
Appendix 1: MTF Data for Red System



MTF – 500 nm



MTF – 700 nm



MTF – 900 nm